An intrinsically disordered region of Drosha selectively promotes miRNA biogenesis, independent of tissue-specific Microprocessor condensates

Bing Yang[1]; Brian Galletta[2]; Rima Sakhawala[1,3]; Nasser Rusan[2] and Katherine McJunkin[1]

[1]National Institute of Diabetes and Digestive and Kidney Diseases Intramural Research Program, National Institutes of Health, 50 South Drive, Bethesda, MD 20815

[2]National Heart, Lung, and Blood Institute, National Institutes of Health, 10 Center Drive, Bethesda, MD 20815

[3]Johns Hopkins University, 3400 North Charles Street, Baltimore, MD 21218

Abstract

Precise control of miRNA biogenesis is of extreme importance, since mis-regulation of miRNAs underlies or exacerbates many disease states. The Microprocessor complex, composed of DROSHA and DGCR8, carries out the first cleavage step in canonical miRNA biogenesis. Despite recent advances in understanding the molecular mechanism of Microprocessor, the N-terminal region of DROSHA is less characterized due its high intrinsic disorder. Here we demonstrate that Microprocessor forms condensates with properties consistent with liquid-liquid phase separation (LLPS) in select tissues in *C. elegans*. While DRSH-1/Drosha recruitment to granules is only partially dependent on its intrinsically disordered regions (IDRs), one of these N-terminal IDRs is crucial for biogenesis of a subset of miRNAs and normal development. A cis region of IDR-dependent miRNAs confers IDR-dependence to another miRNA, suggesting that the IDR recognizes sequences or structures in the miRNA primary transcript. Future studies will further elucidate the specificity of this interaction and the putative role of Microprocessor condensates.

Introduction

microRNAs (miRNAs) are a class of small non-coding RNAs around 22-23 nucleotides in length (Bartel, 2018). Their biogenesis starts with transcription of primary miRNA transcripts (Cai et al., 2004; H. Kim et al., 2024; Lee et al., 2004) which are then recognized and cleaved by the Microprocessor complex composed of DROSHA and DGCR8 (also known as PASH-1 in *C. elegans*) resulting in precursor miRNAs with sizes from ~60 to 80nt (Denli et al., 2004; Gregory et al., 2004; Han et al., 2004, 2006; H. Kim et al., 2024; Landthaler et al., 2004; Lee et al., 2003; Zeng et al., 2005). The precursor miRNA is then exported from the nucleus to the cytoplasm by exportins (Bohnsack et al., 2004; Büssing et al., 2010; Lund et al., 2004; Yi et al., 2003; Zeng & Cullen, 2004). In the cytoplasm, endonuclease DICER recognizes and cleaves the precursor into a mature miRNA duplex (Bernstein et al., 2001; Grishok et al., 2001; Hutvágner et al., 2001; Ketting et al., 2001; Knight & Bass, 2001), which is then loaded into an Argonaute protein to form the miRNA induced silencing complex (miRISC) and target downstream mRNA molecules for gene silencing (Gregory et al., 2005; Grishok et al., 2001; Hammond et al., 2001; Mourelatos et al., 2002; Tabara et al., 1999).

Primary miRNA (pri-miRNA) recognition and cleavage is orchestrated by the Microprocessor complex (Denli et al., 2004; Gregory et al., 2004; Han et al., 2004, 2006; H. Kim et al., 2024; Landthaler et al., 2004; Lee et al., 2003; Zeng et al., 2005). Structural and *in vitro* biochemical studies have intensively characterized the interaction interfaces between the Microprocessor complex and the pri-miRNA molecule; this work has revealed several sequence elements that define substrate optimality of pri-miRNAs, such as the UG motif near the basal junction (Auyeung et al., 2013; Fang & Bartel, 2015; Garg et al., 2024; Jin et al., 2020; B. Kim et al., 2017; Kwon et al., 2016; Li et al., 2020; T. A. Nguyen et al., 2015; Partin et al., 2020). However, most of these studies were carried out using truncated DROSHA without the N-terminus due to aberrant aggregation of the full-length protein (T. A. Nguyen et al., 2015). Therefore, in contrast to the

intensive characterization of the enzymatic domains, the function of the N-terminus of DROSHA is poorly understood. The N-terminal region of DROSHA is the least conserved region of the protein (B. Kim et al., 2017). In vertebrates, the N-terminus is highly enriched in prolines, arginines, and serines, and enriched in overall disorderedness (Son et al., 2023). Global miRNA deficiency was observed upon endogenous deletion of the DROSHA N-terminus (A.A. 1-396) through CRISPR in cell lines (Prabhakar et al., 2023). Another recent report identified a major proteolytic DROSHA isoform that lacks the N-terminal proline-rich disordered domain (PRD – A.A. 1~198) and described the function of the PRD in mediating pri-miRNA processing of a subset of miRNAs encoded in introns (Son et al., 2023).

Over the last decade, liquid-liquid phase separation (LLPS) has been linked to numerous biological phenomena, and LLPS is thought to be the driving force behind the formation of a diverse array of membrane-less organelles, such as stress granules, P-bodies, paraspeckles, and P granules (Banani et al., 2017; Brangwynne et al., 2009). Scaffold molecules initiate the formation of the scaffold matrix through multivalent interactions and then recruit client molecules to further mature these condensates (Banani et al., 2016). Intrinsically disordered regions (IDR) of proteins are hypothesized to be one of the main providers of multivalency (Mitrea & Kriwacki, 2016). Liquid-like biomolecular condensates have been proposed to support diverse functions such as compartmentalization and concentration of biochemical reactions or storage of macromolecules (Putnam et al., 2023). A key question in the field is how frequently observable biomolecular phase-separated droplets represent "incidental condensates" that do not add functionality beyond that provided by the soluble population of proteins outside of the condensates (Putnam et al., 2023).

In this study, we describe nuclear condensate formation of the Microprocessor complex in select *C. elegans* tissues. FRAP experiments suggest that the Microprocessor foci are dynamic, consistent with formation through LLPS. Based on co-localization analysis, we conclude that these DRSH-1 condensates are distinct from known nuclear granules. We then investigate the function of the predicted IDRs in regulating DRSH-1 condensate formation and miRNA biogenesis. We observe that an IDR is required for the biogenesis of a subset of miRNAs and for normal development. However, the roles of the Drosha IDR in miRNA biogenesis and animal development appear to be independent of the condensate formation.

Results

Drosha forms distinct nuclear condensates in *C. elegans*

To assess the distribution of the Microprocessor in *C. elegans*, we fused GFP to the DRSH-1 C-terminus or mCherry to the PASH-1 C-terminus by knock-in at the respective endogenous locus using CRISPR/Cas9 (Figure 1A). To ensure the normal functionality of the fluorescently tagged proteins, we performed co-immunoprecipitation of DRSH-1::GFP and PASH-1::mScarlet and observed a strong interaction, as expected of a functional Microprocessor complex (Figure S1A). To further ensure that the tagged Microprocessor exhibits wild type function at the molecular level,

92 we prepared small RNA libraries from these fluorescently tagged strains, including *drsh-1::gfp,*
93 *pash-1::mScarlet* and *drsh-1::gfp pash-1::mScarlet*, and sequencing revealed no significant
94 changes of miRNA levels when compared to wild type animals (Figure S1B-D, Table S16-18).
95 Thus, these endogenously tagged Microprocessor components function in a wild type manner in
96 miRNA biogenesis.
97
98 Next, we imaged live animals to characterize the distribution of Microprocessor. As expected, we
99 observed DRSH-1::GFP localization primarily in the nucleus across different tissues (Figure 1B).
100 In most tissues, the nuclear DRSH-1::GFP signal was diffuse (e.g. germ line in Figure 1B).
101 Interestingly, we found prominent granule-like distribution of DRSH-1 in nuclei of early embryos
102 and nuclei of both larval and adult hypodermis cells (Figure 1C). The diameter of these granules
103 ranges from those at the diffraction limit (≤250nm) up to ~1μm (Figure S2A). The proportion of
104 DRSH-1::GFP that was localized to the granules was ~2% of the total nuclear signal in the
105 hypodermal cells (Figure S2B). To rule out that GFP contributes to granule formation, we also
106 tagged DRSH-1 with highly monomeric mScarlet (Bindels et al., 2017) and consistently saw
107 granule-like distribution in early embryo and larval and adult hypodermal nuclei (Figure S2C).
108 Imaging of DRSH-1::mScarlet co-expressed with GFP::H2B shows the distribution of these
109 granules throughout the nucleoplasm (Figure S2D). To determine whether the DRSH-1 granules
110 contain both components of the Microprocessor, we generated a double tagged *drsh-1::gfp; pash-*
111 *1::mscarlet* strain and observed strong co-localization of DRSH-1::GFP and PASH-1::mScarlet in
112 these granules (Figure 1D). Taken together, the Microprocessor complex clusters in bright granule-
113 like foci in specific tissues.
114
115 Given the granule-like distribution pattern, we wondered whether these granules are LLPS-
116 mediated biomolecular condensates. To test this hypothesis, we performed fluorescence recovery
117 after photobleaching (FRAP) experiments to bleach an entire focus and monitor fluorescence
118 recovery by the influx of DRSH-1::GFP from the surrounding nucleoplasm. DRSH-1::GFP foci
119 recovered quickly after bleaching ($t_{1/2}$ = 4s ± 0.9s, SEM, n=23) with the intensity recovered to
120 around 50% of the pre-bleaching level, indicating that the condensates consist of both a mobile
121 fraction that exchanges with the nucleoplasmic fraction rapidly and also an immobile DRSH-
122 1::GFP fraction that exchanges very slowly or not at all (Figure 1E-G). While this rapid FRAP is
123 consistent with LLPS of DRSH-1::GFP foci, other mechanisms are also possible. Notably, while
124 the use of live animals allows imaging of many tissues and discovery of tissue-specific foci, the *in*
125 *vivo* system also limits our further characterization of the putative phase separation of the foci
126 (such as via treatment with 1,6-hexanediol or biophysical approaches).
127
128 To determine if DRSH-1 granules coincide with known nuclear granules, we imaged fluorescently-
129 tagged DRSH-1 alongside markers of nuclear granules: paraspeckles marked by NONO-1::GFP,
130 nuclear stress granules labeled by HSF-1::GFP, RNA polymerase II transcriptional condensates
131 marked by AMA-1::GFP, FUS granules labeled by FUST-1::GFP, splicing bodies marked by FOX-

1::GFP, and heterochromatic foci marked by MET-2::mKate (Hills-Muckey et al., 2022; Pham et al., 2021). Although a previous report suggested that DGCR8 localizes to paraspeckles (Jiang et al., 2017), we failed to observe co-localization of either Microprocessor subunit with NONO-1 foci (Figure 1H and S2F). Furthermore, we did not observe any co-localization between DRSH-1 and other known nuclear granule markers (Figure 1H and S2E-F), with the exception of methyltransferase MET-2, where colocalization was only rarely observed: 17% (10 out of 59) of DRSH-1 granules colocalized with MET-2 (Figure S2G). In conclusion, we have found that the Microprocessor complex forms distinct nuclear foci in select tissues in *C. elegans* possibly through LLPS.

DRSH-1 is a client protein in granule formation

Because we observed DRSH-1 granules that are distinct from known nuclear granules, we interrogated whether DRSH-1 itself is the driver of the putative LLPS or rather a client of a condensate formed by another scaffold molecule. If DRSH-1 is the driver of its own phase separation, then all DRSH-1 above the protein's characteristic saturation concentration (c_{sat}) would phase separate and the nucleoplasmic level would be at or below c_{sat}. This would predict that tissues with observable DRSH-1::GFP foci have higher overall nuclear concentration of DRSH-1::GFP than tissues lacking DRSH-1::GFP foci. When we quantified the mean DRSH-1::GFP intensity in nuclei of hypodermis cells and adjacent germ cells (which lack DRSH-1::GFP foci), no significant difference of the average intensities was observed (Figure S2H-I). This observation suggests that granule formation is not solely due to DRSH-1::GFP protein concentration, and DRSH-1 is an LLPS client protein in hypodermal nuclei. However, because only ~2% of DRSH-1::GFP resides in foci in hypodermal nuclei (Figure S2C), very small differences in concentration (as little as 2% higher in hypodermal nuclei) could underlie tissue specificity of granule formation; our detection method may not be sensitive enough to distinguish such small differences.

To further test whether granule formation depends on DRSH-1 concentration, we genetically controlled the concentration of DRSH-1. To this end, we engineered a situation in which the *drsh-1::gfp* allele is heterozygous with a *drsh-1* null allele (hemizygous), thus resulting in lower concentration of DRSH-1::GFP (Figure 2A). We then characterized the hemizygous strain in comparison to its homozygous *drsh-1::gfp* parental strain. In the hemizygous strain, we observed that the overall hypodermal nuclear signal of DRSH-1 was reduced to about 60% of the control (Figure 2B-C). If DRSH-1::GFP granule formation in the wild type setting is driven by DRSH-1::GFP exceeding its c_{sat} by ~2%, then DRSH-1::GFP granules would be abolished in the hemizygous setting which reduces DRSH-1::GFP concentration well below the theoretical c_{sat}. Instead, granules were still formed, though their intensity was reduced to a similar extent as the overall nuclear signal (Figure 2C-D). Reduced granule intensity in the hemizygous background held true when quantifying all foci together (Figure S3A) or when comparing the first or second brightest focus in each nucleus (Figure 2D, Figure S3A). (Intensity was the most accurate measurement of granule formation; we were unable to accurately measure granule size due the

diffraction limit, and we were unable to precisely count granule number as many granules were not much brighter than the nucleoplasm, preventing accurate image thresholding.) Overall, DRSH-1::GFP does not obey a simple c_{sat} predictive model, and thus it likely is a client of other molecules in its recruitment to granules in specific tissues.

A previous study showed that expression of a large miRNA cluster attracted an immobile aggregate of Microprocessor to the genomic locus (Bellemer et al., 2012). To determine whether high expression of clustered miRNAs may also drive the tissue-specific Microprocessor condensate formation observed here, we examined the relative expression of clustered miRNAs in a condensate-forming (hypodermis) and non-condensate forming (neuron) tissue, based on tissue-specific miRNA sequencing (Wang et al., 2024). We observed no enrichment of clustered miRNA expression in hypodermis relative to neuron, providing no support for the possibility of clustered miRNA expression driving tissue-specific Microprocessor condensates (Figure S3C).

Deletion of DRSH-1 IDRs reduces but does not abolish granule recruitment of DRSH-1

The N-terminal region of DROSHA contains intrinsically disordered regions and is proline-enriched (Son et al., 2023). Although the proline-enriched nature is not conserved in *C. elegans* DRSH-1, the disorderedness is conserved (Son et al., 2023). Numerous reports have established the significant contribution of IDRs to LLPS (Dignon et al., 2020); therefore we wondered whether the IDRs of DRSH-1 are important for mediating the recruitment of Microprocessor to granules. To understand the function of the N-terminus of DRSH-1 in its distribution and functionality, we utilized IUPred to predict disorderedness of the region and identified two putative disordered domains (Erdős & Dosztányi, 2020; Mészáros et al., 2018), namely IDR1 and IDR2 (Figure 3A). We used CRISPR to establish mutants in which IDR1, IDR2, or both IDRs are deleted, in both wild type and *drsh-1::gfp* backgrounds. Using the different IDR deletions in the *drsh-1::gfp* background, we assayed the expression of these truncated proteins through western blotting. Migration of the truncated proteins was consistent with their expected sizes. The mutations did not have significant effects on DRSH-1::GFP protein level in the whole animal samples (Figure 3B).

To understand the impact of the IDR deletions on the granule recruitment of DRSH-1::GFP, we imaged the hypodermal nuclei of each of the mutants and compared them to wild type. Overall nuclear signal was slightly reduced in ΔIDR1, slightly increased in ΔIDR2, and similar to wild type in the ΔIDR1/2 background (Figure 3D). (Although these results partially agree with trends observed by western blot, differences are likely due to the difference in sample type: whole animal samples with mixed tissues for western blot versus hypodermal tissue nuclei for imaging.) We found that ΔIDR1 results in slightly lower intensities of granules than wild type; this was the case either when quantifying all foci together (Figure S4A) or when comparing the first or second brightest focus in each nucleus (Figure 3E, S4B). If the IDR1 has a direct role in DRSH-1 recruitment to granules, then its effect on granule intensity should be greater than that of the hemizygous genotype, which had a similar impact as ΔIDR1 on overall nuclear signal (reducing it

212 to 60% of wild type). However, the reduction in granule intensity was comparable to that in the
213 hemizygous background (Figure 3E, Figure 2D), suggesting that the IDR1 itself has no impact on
214 granule recruitment beyond its effect on DRSH-1::GFP concentration. The ΔIDR2 mutation alone
215 did not significantly affect the intensity of all foci quantified together (Figure S4A) and had
216 inconsistent impacts on the intensity of the two brightest granules per nucleus (Figure 3E, Figure
217 S4B). Finally, the ΔIDR1/2 combined mutation reduced granule intensity without affecting overall
218 nuclear DRSH-1::GFP signal (Figure 3D-E, Figure S4). Because the combined mutation – but not
219 the single IDR deletions – decouples granule intensity from DRSH-1::GFP level (reducing
220 intensity without affecting level), this suggests that the two IDRs may act redundantly to promote
221 granule recruitment. This reduction in granule intensity is again mild, indicating that the IDRs are
222 not strictly required for granule recruitment of DRSH-1::GFP, and other parts of the protein also
223 likely contribute. Overall, the IDR mutations had moderate impacts on granule formation, which
224 in the case of ΔIDR1 reflected its impacts on DRSH-1::GFP level.
225
226 **An IDR is important for biogenesis of a subset of miRNAs in *C. elegans***
227 Despite the modest impact of individual IDR mutations on DRSH-1 level and granule recruitment,
228 we observed a strong impact on development in ΔIDR1 mutant animals. The ΔIDR1 but not
229 ΔIDR2 animals showed bursting (vulval rupture) with 9% penetrance, while ΔIDR2 animals were
230 superficially wild type (Figure 4A and 4B). Similar results were obtained when the deletions were
231 introduced in wild type or *drsh-1::gfp* backgrounds, confirming not only the phenotype but also
232 the functionality of the *gfp* tagged DRSH-1 protein (Figure 4B). No other phenotypes were
233 observed; non-bursting ΔIDR1 animals exhibited wild type egg retention, brood size and
234 embryonic viability (Figure S5A-C). The ΔIDR1/2 double mutant mirrored the ΔIDR1 phenotype
235 with 9% penetrance of bursting, indicating that IDR1 and IDR2 do not act redundantly with respect
236 to this aspect of development (Figure 4B).
237
238 The vulval bursting phenotype we observed is reminiscent of loss-of-function mutations in the
239 miRNA pathway (Grishok et al., 2001; Reinhart et al., 2000). To examine the impact of the IDRs
240 on miRNA biogenesis, we performed small RNA sequencing of the ΔIDR1 and ΔIDR2 mutants at
241 the fourth larval (L4) and adult stages. Sequencing analysis using either total piRNAs or spike-ins
242 as a normalization method showed very similar differential expression results (Figure 4 and S5D,
243 Table S5-S12). Among a total of ~200 miRNAs detected by sequencing (DEseq2 normalized mean
244 reads > 5), 49 miRNAs were significantly downregulated in ΔIDR1 in comparison to wild type
245 (DEseq2 $\log_2 FC < -1$, $p_{adj} < 0.05$) at the L4 stage, and only two miRNAs were upregulated ($\log_2 FC >$
246 1, $p_{adj} < 0.05$) (Figure 4C, Table S5). Moreover, we observed a very similar pattern of expression
247 changes in ΔIDR1 animals compared to wild type at the adult stage, with 41 miRNAs
248 downregulated and two upregulated (Figure 4D, Table S6). Changes in miRNA levels caused by
249 ΔIDR1 were highly correlated between the two stages (Figure 4E), with 80% of the downregulated
250 miRNAs in common between L4 and adult (Fisher's exact test $p < 1x10^{-17}$). Thus the ΔIDR1
251 mutation causes a consistent selective defect in miRNA production affecting the same set of

miRNAs across life stages. Among the miRNAs downregulated at both stages are two members of the *let-7* family, *mir-84* and *mir-241*; the downregulation of these miRNAs may be the molecular basis of the bursting phenotype, which is reminiscent of *let-7* family loss of function mutants.

Unlike ΔIDR1 mutants, only minor changes in miRNA profile were observed in the ΔIDR2 mutants, with modest amplitude of changes and poor consistency between life stages (Figure 4F-H, Table S7-S8). In conclusion, IDR1 deletion results in a strong, selective defect in miRNA production across different life stages, whereas IDR2 deletion has little impact.

Next, we sought to determine whether the miRNA abundance changes we observed in ΔIDR1 animals are due to Microprocessor defects rather than other indirect effects. We first validated the downregulation that was observed in deep sequencing for seven mature miRNAs by qPCR (Figure 4I). We also included two miRNAs (*mir-1*, *mir-80*) as controls that were not differentially expressed in the sequencing data, nor were they altered in ΔIDR1 mutants by qPCR (Figure 4I). If the prominent downregulation of select miRNAs observed in ΔIDR1 animals is due to a defect in Microprocessor activity, then decreased mature miRNA levels should be accompanied by increased pri-miRNA levels. We measured pri-miRNA levels by qPCR and observed that this is the case: in all examined cases in which the mature miRNA decreased in ΔIDR1, the corresponding pri-miRNA level increased (Figure 4J). Furthermore, the examined mature miRNAs that were not sensitive to ΔIDR1 (*mir-1, mir-80*) also showed no changes in pri-miRNA level (Figure 4J). Overall, this suggests that DRSH-1 IDR1 is crucial for the efficient Microprocessing of a select subset of miRNAs.

Importantly, neither the bursting phenotype nor the molecular phenotype were due to IDR1's effect on DRSH-1 level or granule recruitment, since neither phenotype was observed in the DRSH-1::GFP hemizygous setting which displayed similar reduction in DRSH-1::GFP levels and granule recruitment as in ΔIDR1 (Figure 2). Small RNA sequencing revealed that the 60% dosage of DRSH-1::GFP and resulting lower granule intensity in the DRSH-1::GFP hemizygous setting did not result in significant changes in miRNA expression profile (Figure S3B, Table S15). Moreover, the hemizygous worms were superficially wild type without any noticeable phenotypes (no bursting). Therefore, the effects of the ΔIDR1 mutation are not recapitulated by orthogonal means of reducing protein dosage and granule recruitment, demonstrating instead that the IDR1 plays a specific role in Microprocessor-mediated cleavage of select substrates.

IDRs have minimal impacts on cleavage site fidelity, except for *mir-259*

We next examined the impact of IDR deletions on cleavage precision by Microprocessor. While the small RNA sequencing method used above (NEBNext) allows for accurate comparison of miRNA expression levels between genotypes, this method suffers from sequence-dependent bias

292 in adaptor ligation efficiency, which confounds comparison of different miRNAs or miRNA
293 isomers (isomiRs) to each other. Therefore, to assess cleavage precision, we performed bias-
294 minimized small RNA sequencing, in which degenerate bases at the ligated end of the library
295 construction adaptors allow for equalized cloning efficiency of different miRNA sequences (H.
296 Kim et al., 2019; Mandlbauer et al., 2024). As expected, the bias-minimized method showed very
297 similar differential expression results when comparing genotypes (ΔIDR1 or ΔIDR2 adults to wild
298 type) (Figure S5E, Table S13-S14).
299
300 Next, we globally examined the cleavage fidelity in wild type and ΔIDR1 or ΔIDR2. We divided
301 the analysis into 5p-derived miRNA strands – of which Microprocessor-mediated cleavage
302 generates the 5' end – and 3p strands, of which Microprocessor cleaves the 3' end (Kwon et al.,
303 2019a) (Figure 5A). Apparent fidelity of Microprocessor cleavage (% with the canonical end
304 position, set as position 0) was higher for 5p strands than 3p strands (Figure 5B, Figure S6).
305 However, miRNA 3' ends (the position assessed for the 3p strands) are known to undergo
306 remodeling that includes exonucleolytic trimming and enzymatic tailing, which cannot be
307 distinguished from Microprocessor cleavage imprecision if the trimmed/tailed isomer still fully
308 matches the genome-encoded sequence. Therefore, we interpret the greater degeneracy in 3p strand
309 3' end position to reflect tailed and trimmed isoforms. Next, we focused on the miRNAs that are
310 downregulated in ΔIDR1. These miRNAs did not display significant differences in the position of
311 their Microprocessor-cleaved ends, with the exception of *mir-54*, suggesting that their
312 downregulation is due to loss of Microprocessor cleavage efficiency, not loss of precision (Figure
313 5C). Since *mir-54* is a 3p-derived miRNA, the shift in its 3' end position could be due to a shift in
314 Microprocessor cleavage position or due to more prevalent terminal uridylation, the most common
315 form of miRNA tailing in *C. elegans* (Vieux et al., 2021) .
316
317 We next extended our analysis to all miRNAs by comparing the cleavage fidelity (% canonical
318 cleavage site) between wild type and ΔIDR1 or ΔIDR2. Only one miRNA showed a significant
319 decrease in cleavage fidelity, *mir-259*, which showed shifted end positions in ΔIDR1. Both strands
320 of *mir-259* were affected, suggesting a greater frequency of Microprocessor cleavage shifted 1bp
321 toward the basal junction relative to the canonical cleavage site in ΔIDR1 (Figure 5A, C). While
322 future work may elucidate what renders the pri-*mir-259* cleavage fidelity sensitive to IDR1, it
323 remains the exception, and generally the impact of IDR1 on miRNAs is solely through changes in
324 abundance, not cleavage position.
325
326
327 ***Cis* sequences of primary *mir-241* confer sensitivity to IDR1 deletion**
328 We observed that ΔIDR1 mutation in DRSH-1 induces a consistent defect in Microprocessing
329 affecting a subset of pri-miRNA substrates; we therefore sought to understand what underlies the
330 specificity of dependence upon the IDR1 for biogenesis. To this end, we tested the association
331 between various features of pri-miRNAs and their sensitivity to the IDR1 deletion (Figure 6A).

332 Although multiple sequence motifs associated with optimal Microprocessor primary miRNA
333 substrates are well annotated in mammalian cells (Auyeung et al., 2013; Fang & Bartel, 2015; Jin
334 et al., 2020; Kwon et al., 2016, 2019b; T. A. Nguyen et al., 2015; Partin et al., 2017), most of these
335 motifs are not enriched in *C. elegans* pri-miRNAs, with the exception of the midBMW and mGHG
336 motifs (Kwon et al., 2019b; Li et al., 2020, 2021), neither of which predicted dependency on IDR1
337 (Figure S7A-B). A recent effort to characterize the *C. elegans* Microprocessor *in vitro* has
338 advanced our understanding of its cleavage parameters and identified a DROSHA dsRNA
339 recognition sites (DRES) motif that correlates with substrate optimality (T. L. Nguyen, Nguyen,
340 Ngo, & Nguyen, 2023; T. L. Nguyen, Nguyen, Ngo, Le, et al., 2023). We examined whether the *in*
341 *vitro* Microprocessor cleavage score or the DRES score were correlated with miRNA sensitivity
342 to ΔIDR1 and again found no association (Figure 6B-C, S7C).
343
344 We then analyzed the features of primary miRNA secondary structure predicted by miRGeneDB
345 (Clarke et al., 2025), including apical loop length, stem length, mismatch count, lower stem length,
346 and bulges. However, no significant correlation was observed between any of these structural
347 features and ΔIDR1 sensitivity (Figure 6D and S7D-E). Additionally, we considered the genomic
348 contexts of pri-miRNAs, including clustering status and intronic/exonic position that were
349 previously reported to be important for the processing of certain subsets of miRNAs (Donayo et
350 al., 2019; Fang & Bartel, 2020; Hutter et al., 2020; Janas et al., 2011; Lataniotis et al., 2017;
351 Pawlicki & Steitz, 2008; Shang et al., 2020; Slezak-Prochazka et al., 2013; Thivierge et al., 2024;
352 Truscott et al., 2016). Moreover, the N-terminus proline-enriched domain of human DROSHA has
353 been shown to mediate intronic miRNA biogenesis (Son et al., 2023). However, our analysis did
354 not show any significant difference in ΔIDR1 sensitivity between these miRNA categories (Figure
355 6E).
356
357 At the organismal level, miRNA expression is known to be spatially regulated and often exhibit
358 tissue and cell-type specificity (Aboobaker et al., 2005; Alberti et al., 2018; Brosnan et al., 2021;
359 Landgraf et al., 2007; Martinez et al., 2008). Given that we observed tissue-specific formation of
360 granules and obvious developmental phenotypes related to hypodermal cells, we wondered
361 whether tissue of expression could contribute to ΔIDR1 sensitivity. To test this hypothesis, we
362 replaced the upstream sequence of an ΔIDR1-insensitive miRNA (*mir-80*) with the upstream
363 sequences of an ΔIDR1-sensitive miRNA (*mir-241*). Intriguingly, we noticed that this ~2kb
364 fragment conferred ΔIDR1 sensitivity to *mir-80* (Figure 6F, mut1). To determine whether this
365 fragment conferred sensitivity by driving *mir-80* expression in the hypodermis, we then replaced
366 the sequence upstream of *mir-80* with a known hypodermis promoter (*dpy-7*), but this did not
367 confer sensitivity to ΔIDR1 to *mir-80* to the same extent as the 2kb *mir-241* upstream fragment
368 (Figure 6F, mut2). We thus revisited the 2kb sequence and divided it into the 1.7kb fragment
369 upstream of the pri-*mir-241* TSS (R. A.-J. Chen et al., 2013; Gu et al., 2012; Kruesi et al., 2013;
370 Saito et al., 2013) and the remaining 293bp that lies between the TSS and the predicted basal
371 junction of pri-*mir-241*. We then replaced the corresponding fragments in the *mir-80* locus with

372 the fragments of the *mir-241* locus. Strikingly, the 293bp cis element, but not the 1.7kb upstream
373 fragment conferred sensitivity of *mir-80* to ΔIDR1 (Figure 5F, mut4 and mut3), similar to the full
374 2kb fragment of *mir-241*. To confirm that the 5' flanking sequence is conferring IDR1 sensitivity,
375 we replaced the 293bp fragment of *mir-80* with one from another IDR-sensitive miRNA, *mir-54,*
376 and again observed conferral of IDR1-dependence (Figure 6F, mut5). To determine whether the
377 sequence swaps interfered with the canonical cleavage of *mir-80* in the variant genetic
378 backgrounds, we prepared small RNA libraries using the bias-minimized cloning method. This
379 analysis recapitulated the *mir-80* abundance changes detected through miRNA Taqman qPCR
380 (Figure S8A), and the cleavage patterns were highly canonical for all *mir-80* variant loci,
381 suggesting that – similar to wild type IDR1-sensitive loci – the IDR1-sensitive variants of pri-*mir-*
382 *80* rely on IDR1 for efficiency, not precision, of Microprocessor-mediated cleavage (Figure S8B).
383 Together, this suggests that flanking sequences near the base of the pri-miRNA hairpin determine
384 dependence on DRSH-1 IDR1 for maximally efficient processing.
385
386 **Discussion**
387 In this study, we describe the formation of distinct nuclear DRSH-1 foci in select tissues in *C.*
388 *elegans*, consistent with recruitment to LLPS condensates. Although a previous report hinted at
389 the potential co-localization between DGCR8 and paraspeckles (Jiang et al., 2017), our study
390 provides the first evidence of Microprocessor condensates in animals. We demonstrate that DRSH-
391 1 is a client protein in condensate formation since the simple phase separation model defined
392 by $>c_{sat}$ of DRSH-1 is incompatible with the behavior of these granules. What scaffolds
393 Microprocessor foci and governs their tissue specificity will be a crucial question as more
394 components of these granules are identified. The current study is also limited by the diffraction
395 limit (~250nm) of our imaging methods; further characterization of the granules by super
396 resolution microscopy will provide finer details of the condensates' structure and potentially
397 identify smaller-scale clusters in tissues other than embryos and hypodermal cells. Which regions
398 of DRSH-1 itself are required for its recruitment to granules is another open question; the N-
399 terminal IDRs redundantly promote DRSH-1 granule recruitment, but their impact is modest,
400 suggesting other regions of the protein also support recruitment.
401
402 The ability of Microprocessor to be recruited to condensates may provide a new layer of
403 Microprocessor regulation that was not previously explored. A lack of conditions in which granule
404 formation is completely abolished limits our ability to assess their function. One possibility is that
405 the Microprocessor condensates are "incidental condensates" resulting from the biophysical
406 properties of the complex and the nuclear context but not providing functionality beyond that of
407 diffuse Microprocessor (Putnam et al., 2023). Understanding the factors involved in scaffolding of
408 Microprocessor-containing granules will aid in perturbing these foci to probe their function.
409
410 Whereas the DRSH-1 IDRs had a modest role in Microprocessor recruitment to granules and
411 modest effects on DRSH-1 concentration, IDR1 clearly contributes to Microprocessor function.

412 The ΔIDR1 mutants exhibited strong molecular and developmental phenotypes related to
413 Microprocessing defects.
414
415 The hypodermis is both a site of apparent Microprocessor condensates and the tissue of origin of
416 the ΔIDR1 mutant phenotype. This led us to interrogate the relationship of these phenomena. Using
417 genetics, especially the implications of the DRSH-1 hemizygous setting, we were able to separate
418 the IDR1 function in biogenesis from DRSH-1 focus formation. The DRSH-1 hemizygous setting
419 demonstrates that enforcing a modest reduction in DRSH-1 concentration and focus formation –
420 comparable to those observed in the ΔIDR1 background – does not necessarily lead to defects in
421 Microprocessing. We propose that careful modulation of protein concentration can be a general
422 means for avoiding guilt-by-association between specific IDR-driven molecular processes and co-
423 occurring LLPS.
424
425 We have shown that DRSH-1 IDR1 strongly contributes to biogenesis of a subset of miRNAs,
426 independent of known features of *C. elegans* Microprocessor substrate optimality. The 5' flanking
427 region of two IDR1-sensitive miRNAs each conferred sensitivity to an IDR1-insensitive miRNA;
428 these interesting observations suggest that a cis-acting element in this region of the pri-miRNA
429 could be interacting with the IDR1 domain. The fact that miRNAs derived from the same primary
430 transcript behaved differentially in response to IDR1 deletion – i.e. *mir-54* is significantly IDR1-
431 sensitive, whereas both *mir-55* and *mir-56* did not respond to IDR1 deletion (Figure S9) – further
432 supports the model that a cis element very close to the miRNA hairpin could mediate IDR1-
433 dependence. So far, our attempts at motif finding and structural prediction have not yielded
434 candidate cis elements whose functionality can be tested. Our findings are interestingly similar to
435 the involvement of cis elements in determining pri-miRNA reliance on the N-terminal IDRs of
436 human DROSHA, suggesting that these sequence-divergent regions of orthologous proteins may
437 maintain conserved function (Son et al., 2023). Future studies using high-throughput functional
438 genomics should reveal what properties define the sequence or structural feature that is recognized
439 by the IDR domain and whether the recognition is direct or indirect through other RNA binding
440 proteins (Figure 7).
441
442 **Materials and Methods**
443 ***C. elegans* culture**
444 *C. elegans* were cultured using standard protocols at 20°C (Stiernagle, 2006). L4 and adult worm
445 samples were collected 48 h and 60 h after L1 synchronization, respectively.
446
447 **Genome editing**
448 Unless otherwise mentioned, strains generated in this study were engineered endogenously using
449 CRISPR-Cas9. CRISPR-Cas9 mediated genome editing is performed as previously reported (Yang
450 et al., 2020). In brief, IDT alt-R guide RNAs were annealed by mixing crRNA and tracrRNA to a
451 final concentration of 10μM each using IDT duplex buffer, which was then incubated at 95°C for

452 5 min followed by gradual temperature decline to room temperature. Repair templates provided
453 for CRISPR were column purified after PCR synthesis. Final injection mix contains annealed
454 gRNA at final concentration of 1µM, IDT Cas9 at final concentration of 2µM and repair template
455 at final concentration ~200-400ng/µl (Paix et al., 2014). A gRNA targeting *dpy-10* was used as a
456 co-CRISPR marker for selection (Arribere et al., 2014). After injection, Dpy animals were cloned
457 and singled as F1s. F2 animals were then genotyped for desired edits.
458 GFP donor fragments were amplified using plasmid pCM1.35 as a template and primers containing
459 ~35-55 bp homology arms (Merritt et al., 2008; Paix et al., 2014). mScarlet donor molecules were
460 amplified using plasmid pGLOW30 as a template and primers containing ~35-55 bp homology
461 arms (Witten et al., 2023). Promoter sequences of *mir-241*, *mir-84* and *dpy-7* were amplified from
462 wild type genomic DNA using primers listed in table S2. Transcription start sites were determined
463 using the Wormbase TSS database (R. A.-J. Chen et al., 2013; Gu et al., 2012; Kruesi et al., 2013;
464 Saito et al., 2013).
465
466 **Western Blotting**
467 Three 10cm NGM plates seeded with 2,000 L1s were cultured at 20°C for 60 h, until animals
468 reached adulthood. Animals were then rinsed off the NGM plates with M9 buffer and washed three
469 times with M9 before being pelleted and snap frozen. Upon thawing, the worm pellets were mixed
470 with equal volume of cold 2x worm lysis buffer (60 mM HEPES pH 7.4, 100 mM KCl, 0.4%
471 Triton X-100, 4 mM $MgCl_2$, 20% glycerol, 4 mM DTT, 2× cOmplete, Mini, EDTA-free Protease
472 Inhibitor Cocktail) and lysed using a Bioruptor Pico (Diagenode) for 10 cycles (30 seconds on and
473 30 seconds off). Crude worm lysate was then cleared by centrifugation at 16,000x*g* for 10 min.
474 Protein concentration of the resulting supernatant was then quantified using BCA assay. Equal
475 amounts of protein were loaded onto a 4-15% gradient Tris Glycine gel (Biorad). Membranes were
476 then probed with anti-GFP antibody (Roche) at 1:1,000 and anti-tubulin antibody DM1A (Abcam)
477 at 1:1,000.
478
479 **Immunoprecipitation**
480 Worms were harvested from 10cm NGM plates and washed three times with M9 buffer. Worm
481 pellet was flash frozen on dry ice and stored in -80°C until use. Upon thawing, equal volume of
482 2X IP lysis buffer (100mM Tris-HCl, 200 mM KCl, 5mM MgCl2, 0.2% NP-40, 1mM PMSF, 20%
483 glycerol) supplemented with proteinase inhibitor cocktail was added to the worm pellet. Worm
484 lysis was carried out using Bioruptor sonicator with 7 cycles of 30 seconds ON and 30 seconds
485 OFF. Worm lysate was then cleared by centrifugation at 15,000 rpm for 10 minutes. The
486 supernatant was transferred to a new tube and used as input for immunoprecipitation. Proteintech
487 GFP-trap agarose beads (10µl) were added to 2mg of input lysate and incubated at 4˚C for 2 hours
488 on a rotator. Beads were then collected by centrifugation at 1,000rpm for 1 minute, and washed
489 three times with 1X IP lysis buffer. 2X SDS Laemmli sample buffer was added to the beads and
490 incubated at 95˚C for 5 minutes. Western blot was performed as above using anti-GFP antibody
491 (Proteintech anti-GFP PABG1) and anti-RFP antibody (Proteintech anti-RFP 6G6).

492
493 **IsomiR analysis**
494 To analyze isomiR distribution, aligned bam files were converted to fastq and collapsed to tabular
495 files containing read sequence and count information. SeqBuster was then used to annotate
496 miRNAs/isomiRs with the following parameters -sub 0 -trim 3 -add 3 -s cel. Annotation
497 information from miRbase was used as a reference file for seqBuster (Pantano et al., 2010). A
498 custom script was developed to analyze the distribution of isomiRs potentially resulting from
499 variation of Microprocessor cleavage sites. Briefly, miRNAs with baseMean > 25 from DEseq2
500 analysis were included in this analysis. To minimize the confounding effects of miRNA tailing on
501 isomiR distribution, miRNA reads with unambiguous untemplated additions at the 3' end were
502 removed from the analysis.
503
504 **Microscopy**
505 Fluorescent microscopy was performed using a Nikon Eclipse Ti2 microscope (Nikon Instruments,
506 Melville, NY, USA) equipped with a W1 spinning disk confocal head (Yokogawa, Life Science,
507 Tokyo, Japan), 405-, 488-, 561-, and 641-nm laser lines, a 100x/1.49 total internal reflection
508 fluorescence oil immersion objective (Nikon Instruments) and a Prime BSI cMOS camera
509 (Teledyne Photometrics, Tuscon, AZ, USA). Fluorescence recovery after photobleaching (FRAP)
510 was performed using an Opti-MicroScan unit with a 405 nm laser. Nikon Elements software was
511 used to control the microscope and to collect images (Nikon Instruments). Image analysis was
512 performed using FIJI (Image J; National Institutes of Health, Bethesda, MD, USA).
513
514 **FRAP**
515 FRAP experiments were performed using the microscope described above. Hypodermal cells
516 nearest the coverslip were selected for imaging in which a single confocal plane was acquired
517 using 2x2 binning. One prominent fluorescent focus was selected for FRAP using a 10 millisecond,
518 405 nm laser exposure, which was sufficient to partially photobleach the focus. Movies of a single
519 focal plane using the 488nm laser were then collected using 2x2 binning and one image/second.
520 Only movies where the partially photobleached focus stayed within the imaging plane were used
521 for analysis.
522
523 For analysis, total integrated fluorescence measurements of a region of interest including the
524 bleached focus were recorded at each timepoint. Background subtraction was performed using a
525 nuclear region of identical area adjacent to the focus. Correction for photobleaching resulting from
526 timelapse image acquisition using the 488nm laser was performed by using the decrease in
527 fluorescence across the entire image. Data was normalized by setting the average focus intensity
528 from 10 pre-bleach frames to 1, and the first post-bleach frame to 0. The frame containing the
529 bleaching laser pulse was excluded from the analysis. Figure 1F presents the average of all
530 recovery curves ± standard deviation with time 0 equal to 10 frames prior to bleaching. The $t_{1/2}$ of

recovery and immobile fraction from individual recovery curves were determined following fitting (one phase association) using Prism (GraphPad, Boston, MA, USA).

Fluorescence intensity measurements in hypodermal nuclei

Confocal Z-stack images of hypodermal cells close to the coverslip in live worms were acquired using the microscope described above. Only nuclei where the animal and the foci did not move substantially during acquisition were selected for analysis. For measurements of DRSH-1::GFP foci, the integrated fluorescence intensity of a region of interest around prominent foci from a single imaging plane was measured using Image J. An adjacent region within the nucleus that lacks DRSH-1::GFP foci was used for background subtraction. To determine the upper limit of focus intensity per nucleus, the first and second brightest foci from each nucleus were identified and quantified. The dimmest foci in the nucleus occasionally yielded negative values after measurement because their intensity was so close to the noise floor. These foci were excluded from the "All foci" analysis. As a result, "All foci" represents all foci that could be identified and measured. Fluorescence intensity was normalized to the average intensity of the comparable ("brightest or "all") foci in nuclei from wild type DRSH-1::GFP worms during each imaging session.

Measurements of the intensity of GFP in the whole nucleus and estimates of percent DRSH-1::GFP residing in foci both utilized the same images as measurements of foci. However, due to movement of the animals during Z-stack acquisition, only a subset of images could be used for these analyses. Sum projections of the Z-slices containing the nucleus were generated, and the fluorescence intensity of a region of interest containing the nucleus was measured. An adjacent region outside of the nucleus, but within the same cell was used for background subtraction. Fluorescence intensity was normalized to the average intensity of the nuclear GFP signal from wild type DRSH-1::GFP worms for each imaging session. To determine the percentage of DRSH-1::GFP nuclear signal that was in the foci, sum projections were made of each focus in a nucleus, and the fluorescence intensity of a region of interest containing each focus in the resulting images were measured. The sum of all the foci in each nucleus was then calculated and the divided by the total nuclear fluorescence determined above.

Brood size assay and bursting phenotype scoring

Brood size assay was performed as previously described (Kotagama et al., 2024). In brief, L4 animals of each genotype were singled onto individual plates and transferred to fresh plates every 24 h until embryos were no longer produced. Bursting phenotype was assessed within 48 h after animals reached L3 stage.

RNA extraction

Bulk samples of L4 and adult stage animals were pelleted from 10cm NMG plates using M9 and snap-frozen in 500µl TRIzol (Life Technologies) until use. Adult animals for Figures 4 and 5 were

571 handpicked in the quantity of one hundred per sample into 20 µl M9 buffer in Eppendorf tubes,
572 and 500µl TRIzol was added to each tube before snap freezing. Upon thawing, samples were
573 vortexed at room temperature for 15 min. 85 µl chloroform was added to each sample and mixed
574 thoroughly. Samples were then centrifuged at 16,000×*g* for 10 min at 4°C. The supernatant was
575 transferred to a fresh tube and an equal volume of 25:24:1 phenol:chloroform:isoamyl alcohol
576 pH=4.5 was added to the sample. Samples were then centrifuged at 16,000×*g* for 15 min at 4°C.
577 The upper aqueous phase was transferred to a fresh tube and an equal volume of isopropanol and
578 1 µl of GlycoBlue (Thermo Fisher Scientific) was added to the aqueous phase and mixed gently.
579 Samples were frozen at −80°C for 30 min and thawed on ice. RNA precipitation was carried out
580 at 20,000×*g* for 30 min at 4°C. The RNA pellets were then washed twice with 70% ethanol with 5
581 min of centrifugation at 4°C. Approximately 20 µl of RNase-free water was added to resuspend
582 the RNA.
583
584 **qPCR**
585 For miRNA qPCR, reverse transcription reactions were performed using miRNA-specific RT
586 primers with the Taqman microRNA Reverse Transcription (RT) Kit (Thermo Fisher Scientific).
587 For all samples, 1.66 µl of total RNA at 5 ng/µl was used in 5 µl RT reactions. RT reactions were
588 then diluted 1:4 and 1.33 µl was used in a 5 µl qPCR reactions using Taqman miRNA probes and
589 the Taqman Universal Mastermix II with UNG (Thermo Fisher Scientific). Reactions were run in
590 three technical replicates on the Applied Biosystems QuantStudio 6.
591
592 Primary miRNA qPCR was performed using KAPA SYBR Fast One-Step qRT-PCR Kit on
593 QuantStudio 6 Flex Real-Time PCR System using primers listed in Table S2. In brief, 1.33 µl of
594 total RNA 5 ng/µl was used in a 5µl qPCR reaction. Reactions were run in three technical replicates
595 for each sample.
596
597 **Small RNA sequencing and mapping**
598 Small RNA library preparation was adapted from the NEBNext small RNA library prep kit (New
599 England Biolabs) (Vieux et al., 2021). Briefly, spike-ins were added to 600 ng of total RNA prior
600 to library construction for each sample. Size selection was performed after reverse transcription
601 using 8% urea gel to purify 65-75 nt products. PCR was performed with 15 cycles followed by
602 purification using NEB Monarch PCR purification kit to remove primer dimers. Cloned libraries
603 were sequenced on the Illumina NextSeq 2000 platform.
604 For bias-minimized small RNA cloning, libraries were constructed as previously described with
605 minor modifications (Mandlbauer et al., 2024). Briefly, 1 µg of total RNA was used as input, and
606 both 5′ and 3′ adaptors were added at a final concentration of 1µM. Spike-ins were introduced
607 across a range of concentrations as previously reported (Sakhawala et al., 2025). Cloned libraries
608 were then sequenced on the Illumina NovaSeq 6000 platform.
609 Sequence analysis was performed on the NIH high performance computing cluster. Adapter
610 sequences were trimmed using fastp (0.24.0) command fastp -L (S. Chen, 2023). The reference

genome was customized by combining *C. elegans* genome WS280 with an artificial chromosome containing the synthetic spike-in sequences (Donnelly et al., 2022). Mapping was performed using Bowtie2 using the following settings: --end-to-end --sensitive -q -U (Langmead & Salzberg, 2012). BAM files were sorted and indexed using samtools 1.13 (Danecek et al., 2021). Reads were assigned to miRNAs and piRNAs using htseq 0.13.5 (Putri et al., 2022) with the following settings: --mode union --nonunique fraction -a 0. The htseq analysis on miRNAs was performed using a gff file modified from mirGeneDB (Fromm et al., 2015). The htseq analysis on piRNAs was performed using a gff file from https://www.pirnadb.org/ (Piuco & Galante, 2021). miRNA differential gene expression was analyzed using DESeq2 analysis with default settings (Love et al., 2014) using total piRNA reads or spike-in reads for normalization.
For bias-minimized sequencing data, bam files were collapsed using UMI-tools (Smith et al., 2017) and filtered for reads between 16nt and 30nt.

Data availability

All primary sequence data have been deposited at NCBI Gene Expression Omnibus under accession number GSE289120. Reviewers may access the data using the following token: abqnacikpdgltyd.

Competing Interest Statement

The authors have not competing interests to declare.

Acknowledgements

We thank members of the laboratory and Baltimore Worm Club for helpful discussions. We thank Geraldine Seydoux for critical feedback on the manuscript. Multiple strains were obtained from the CGC, which is funded by NIH Office of Research Infrastructure Programs (P40 OD010440). WormBase was used for the design and execution of the study (Sternberg et al., 2024). This research was funded by the NIDDK Intramural Research Program (ZIADK075147) and NHLBI Intramural Research Program (ZIAHL006126).

This research was supported by the Intramural Research Program of the National Institute of Diabetes and Digestive and Kidney Diseases (NIDDK) within the National Institutes of Health (NIH). The contributions of the NIH author(s) were made as part of their official duties as NIH federal employees, are in compliance with agency policy requirements, and are considered Works of the United States Government. However, the findings and conclusions presented in this paper are those of the author(s) and do not necessarily reflect the views of the NIH or the U.S. Department of Health and Human Services."

Author Contributions

B.Y. designed and performed experiments, analyzed the data, and wrote and revised the manuscript. B.G. performed experiments, analyzed data, and helped revise the manuscript. N.R. designed

experiments and helped revise the paper. R.S. designed and performed experiments. K.M designed experiments and wrote and revised the manuscript.

References

Aboobaker, A. A., Tomancak, P., Patel, N., Rubin, G. M., & Lai, E. C. (2005). Drosophila microRNAs exhibit diverse spatial expression patterns during embryonic development. *Proceedings of the National Academy of Sciences of the United States of America*, *102*(50), 18017–18022. https://doi.org/10.1073/pnas.0508823102

Alberti, C., Manzenreither, R. A., Sowemimo, I., Burkard, T. R., Wang, J., Mahofsky, K., Ameres, S. L., & Cochella, L. (2018). Cell-type specific sequencing of microRNAs from complex animal tissues. *Nature Methods*, *15*(4), 283–289. https://doi.org/10.1038/nmeth.4610

Arribere, J. A., Bell, R. T., Fu, B. X., Artiles, K. L., Hartman, P. S., & Fire, A. Z. (2014). Efficient marker-free recovery of custom genetic modifications with CRISPR/Cas9 in Caenorhabditis elegans. *Genetics*, *198*(3), 837–846. https://doi.org/10.1534/genetics.114.169730

Auyeung, V. C., Ulitsky, I., McGeary, S. E., & Bartel, D. P. (2013). Beyond secondary structure: primary-sequence determinants license pri-miRNA hairpins for processing. *Cell*, *152*(4), 844–858. https://doi.org/10.1016/j.cell.2013.01.031

Banani, S. F., Lee, H. O., Hyman, A. A., & Rosen, M. K. (2017). Biomolecular condensates: organizers of cellular biochemistry. *Nature Reviews. Molecular Cell Biology*, *18*(5), 285–298. https://doi.org/10.1038/nrm.2017.7

Banani, S. F., Rice, A. M., Peeples, W. B., Lin, Y., Jain, S., Parker, R., & Rosen, M. K. (2016). Compositional Control of Phase-Separated Cellular Bodies. *Cell*, *166*(3), 651–663. https://doi.org/10.1016/j.cell.2016.06.010

Bartel, D. P. (2018). Metazoan MicroRNAs. In *Cell*. https://doi.org/10.1016/j.cell.2018.03.006

Bellemer, C., Bortolin-Cavaillé, M.-L., Schmidt, U., Jensen, S. M. R., Kjems, J., Bertrand, E., & Cavaillé, J. (2012). Microprocessor dynamics and interactions at endogenous imprinted C19MC microRNA genes. *Journal of Cell Science*, *125*(Pt 11), 2709–2720. https://doi.org/10.1242/jcs.100354

Bernstein, E., Caudy, A. A., Hammond, S. M., & Hannon, G. J. (2001). Role for a bidentate ribonuclease in the initiation step of RNA interference. *Nature*, *409*(6818), 363–366. https://doi.org/10.1038/35053110

Bindels, D. S., Haarbosch, L., van Weeren, L., Postma, M., Wiese, K. E., Mastop, M., Aumonier, S., Gotthard, G., Royant, A., Hink, M. A., & Gadella, T. W. J. (2017). mScarlet: a bright monomeric red fluorescent protein for cellular imaging. *Nature Methods*, *14*(1), 53–56. https://doi.org/10.1038/nmeth.4074

Bohnsack, M. T., Czaplinski, K., & Gorlich, D. (2004). Exportin 5 is a RanGTP-dependent dsRNA-binding protein that mediates nuclear export of pre-miRNAs. *RNA (New York, N.Y.)*, *10*(2), 185–191. https://doi.org/10.1261/rna.5167604

Brangwynne, C. P., Eckmann, C. R., Courson, D. S., Rybarska, A., Hoege, C., Gharakhani, J., Jülicher, F., & Hyman, A. A. (2009). Germline P granules are liquid droplets that localize by controlled dissolution/condensation. *Science (New York, N.Y.)*, *324*(5935), 1729–1732. https://doi.org/10.1126/science.1172046

Brosnan, C. A., Palmer, A. J., & Zuryn, S. (2021). Cell-type-specific profiling of loaded miRNAs from Caenorhabditis elegans reveals spatial and temporal flexibility in Argonaute loading. *Nature Communications*, *12*(1), 2194. https://doi.org/10.1038/s41467-021-22503-7

Büssing, I., Yang, J.-S., Lai, E. C., & Grosshans, H. (2010). The nuclear export receptor XPO-1 supports primary miRNA processing in C. elegans and Drosophila. *The EMBO Journal*, *29*(11), 1830–1839. https://doi.org/10.1038/emboj.2010.82

Cai, X., Hagedorn, C. H., & Cullen, B. R. (2004). Human microRNAs are processed from capped, polyadenylated transcripts that can also function as mRNAs. *RNA (New York, N.Y.)*, *10*(12), 1957–1966. https://doi.org/10.1261/rna.7135204

Chen, R. A.-J., Down, T. A., Stempor, P., Chen, Q. B., Egelhofer, T. A., Hillier, L. W., Jeffers, T. E., & Ahringer, J. (2013). The landscape of RNA polymerase II transcription initiation in C. elegans reveals promoter and enhancer architectures. *Genome Research*, *23*(8), 1339–1347. https://doi.org/10.1101/gr.153668.112

Chen, S. (2023). Ultrafast one-pass FASTQ data preprocessing, quality control, and deduplication using fastp. *IMeta*, *2*(2), e107. https://doi.org/10.1002/imt2.107

Clarke, A. W., Høye, E., Hembrom, A. A., Paynter, V. M., Vinther, J., Wyrożemski, Ł., Biryukova, I., Formaggioni, A., Ovchinnikov, V., Herlyn, H., Pierce, A., Wu, C., Aslanzadeh, M., Cheneby, J., Martinez, P., Friedländer, M. R., Hovig, E., Hackenberg, M., Umu, S. U., … Fromm, B. (2025). MirGeneDB 3.0: improved taxonomic sampling, uniform nomenclature of novel conserved microRNA families and updated covariance models. *Nucleic Acids Research*, *53*(D1), D116–D128. https://doi.org/10.1093/nar/gkae1094

Danecek, P., Bonfield, J. K., Liddle, J., Marshall, J., Ohan, V., Pollard, M. O., Whitwham, A., Keane, T., McCarthy, S. A., Davies, R. M., & Li, H. (2021). Twelve years of SAMtools and BCFtools. *GigaScience*, *10*(2). https://doi.org/10.1093/gigascience/giab008

Denli, A. M., Tops, B. B. J., Plasterk, R. H. A., Ketting, R. F., & Hannon, G. J. (2004). Processing of primary microRNAs by the Microprocessor complex. *Nature*, *432*(7014), 231–235. https://doi.org/10.1038/nature03049

Dignon, G. L., Best, R. B., & Mittal, J. (2020). Biomolecular Phase Separation: From Molecular Driving Forces to Macroscopic Properties. *Annual Review of Physical Chemistry*, *71*, 53–75. https://doi.org/10.1146/annurev-physchem-071819-113553

Donayo, A. O., Johnson, R. M., Tseng, H.-W., Izreig, S., Gariepy, A., Mayya, V. K., Wu, E., Alam, R., Lussier, C., Jones, R. G., & Duchaine, T. F. (2019). Oncogenic Biogenesis of pri-miR-17∼92 Reveals Hierarchy and Competition among Polycistronic MicroRNAs. *Molecular Cell*, *75*(2), 340-356.e10. https://doi.org/10.1016/j.molcel.2019.05.033

Donnelly, B. F., Yang, B., Grimme, A. L., Vieux, K.-F., Liu, C.-Y., Zhou, L., & McJunkin, K. (2022). The developmentally timed decay of an essential microRNA family is seed-sequence dependent. *Cell Reports*, *40*(6), 111154. https://doi.org/10.1016/j.celrep.2022.111154

Erdős, G., & Dosztányi, Z. (2020). Analyzing Protein Disorder with IUPred2A. *Current Protocols in Bioinformatics*, *70*(1), e99. https://doi.org/10.1002/cpbi.99

Fang, W., & Bartel, D. P. (2015). The Menu of Features that Define Primary MicroRNAs and Enable De Novo Design of MicroRNA Genes. *Molecular Cell*, *60*(1), 131–145. https://doi.org/10.1016/j.molcel.2015.08.015

Fang, W., & Bartel, D. P. (2020). MicroRNA Clustering Assists Processing of Suboptimal MicroRNA Hairpins through the Action of the ERH Protein. *Molecular Cell*, *78*(2), 289-302.e6. https://doi.org/10.1016/j.molcel.2020.01.026

Fromm, B., Billipp, T., Peck, L. E., Johansen, M., Tarver, J. E., King, B. L., Newcomb, J. M., Sempere, L. F., Flatmark, K., Hovig, E., & Peterson, K. J. (2015). A Uniform System for the Annotation of Vertebrate microRNA Genes and the Evolution of the Human microRNAome. *Annual Review of Genetics*, *49*, 213–242. https://doi.org/10.1146/annurev-genet-120213-092023

Garg, A., Shang, R., Cvetanovic, T., Lai, E. C., & Joshua-Tor, L. (2024). The structural landscape of Microprocessor-mediated processing of pri-let-7 miRNAs. *Molecular Cell*, *84*(21), 4175-4190.e6. https://doi.org/10.1016/j.molcel.2024.09.008

Gregory, R. I., Chendrimada, T. P., Cooch, N., & Shiekhattar, R. (2005). Human RISC couples microRNA biogenesis and posttranscriptional gene silencing. *Cell*, *123*(4), 631–640. https://doi.org/10.1016/j.cell.2005.10.022

Gregory, R. I., Yan, K.-P., Amuthan, G., Chendrimada, T., Doratotaj, B., Cooch, N., & Shiekhattar, R. (2004). The Microprocessor complex mediates the genesis of microRNAs. *Nature*, *432*(7014), 235–240. https://doi.org/10.1038/nature03120

Grishok, A., Pasquinelli, A. E., Conte, D., Li, N., Parrish, S., Ha, I., Baillie, D. L., Fire, A., Ruvkun, G., & Mello, C. C. (2001). Genes and mechanisms related to RNA interference regulate expression of the small temporal RNAs that control C. elegans developmental timing. *Cell*, *106*(1), 23–34. https://doi.org/10.1016/s0092-8674(01)00431-7

Gu, W., Lee, H.-C., Chaves, D., Youngman, E. M., Pazour, G. J., Conte, D., & Mello, C. C. (2012). CapSeq and CIP-TAP identify Pol II start sites and reveal capped small RNAs as C. elegans piRNA precursors. *Cell*, *151*(7), 1488–1500. https://doi.org/10.1016/j.cell.2012.11.023

Hammond, S. M., Boettcher, S., Caudy, A. A., Kobayashi, R., & Hannon, G. J. (2001). Argonaute2, a link between genetic and biochemical analyses of RNAi. *Science (New York, N.Y.)*, *293*(5532), 1146–1150. https://doi.org/10.1126/science.1064023

Han, J., Lee, Y., Yeom, K.-H., Kim, Y.-K., Jin, H., & Kim, V. N. (2004). The Drosha-DGCR8 complex in primary microRNA processing. *Genes & Development*, *18*(24), 3016–3027. https://doi.org/10.1101/gad.1262504

Han, J., Lee, Y., Yeom, K.-H., Nam, J.-W., Heo, I., Rhee, J.-K., Sohn, S. Y., Cho, Y., Zhang, B.-T., & Kim, V. N. (2006). Molecular basis for the recognition of primary microRNAs by the Drosha-DGCR8 complex. *Cell*, *125*(5), 887–901. https://doi.org/10.1016/j.cell.2006.03.043

Hills-Muckey, K., Martinez, M. A. Q., Stec, N., Hebbar, S., Saldanha, J., Medwig-Kinney, T. N., Moore, F. E. Q., Ivanova, M., Morao, A., Ward, J. D., Moss, E. G., Ercan, S., Zinovyeva, A. Y., Matus, D. Q., & Hammell, C. M. (2022). An engineered, orthogonal auxin analog/AtTIR1(F79G) pairing improves both specificity and efficacy of the auxin degradation system in Caenorhabditis elegans. *Genetics*, *220*(2). https://doi.org/10.1093/genetics/iyab174

Hutter, K., Lohmüller, M., Jukic, A., Eichin, F., Avci, S., Labi, V., Szabo, T. G., Hoser, S. M., Hüttenhofer, A., Villunger, A., & Herzog, S. (2020). SAFB2 Enables the Processing of Suboptimal Stem-Loop Structures in Clustered Primary miRNA Transcripts. *Molecular Cell*, *78*(5), 876-889.e6. https://doi.org/10.1016/j.molcel.2020.05.011

Hutvágner, G., McLachlan, J., Pasquinelli, A. E., Bálint, E., Tuschl, T., & Zamore, P. D. (2001). A cellular function for the RNA-interference enzyme Dicer in the maturation of the let-7 small temporal RNA. *Science (New York, N.Y.)*, *293*(5531), 834–838. https://doi.org/10.1126/science.1062961

Janas, M. M., Khaled, M., Schubert, S., Bernstein, J. G., Golan, D., Veguilla, R. A., Fisher, D. E., Shomron, N., Levy, C., & Novina, C. D. (2011). Feed-forward microprocessing and splicing activities at a microRNA-containing intron. *PLoS Genetics*, *7*(10), e1002330. https://doi.org/10.1371/journal.pgen.1002330

Jiang, L., Shao, C., Wu, Q.-J., Chen, G., Zhou, J., Yang, B., Li, H., Gou, L.-T., Zhang, Y., Wang, Y., Yeo, G. W., Zhou, Y., & Fu, X.-D. (2017). NEAT1 scaffolds RNA-binding proteins and

787 the Microprocessor to globally enhance pri-miRNA processing. *Nature Structural &*
788 *Molecular Biology*, *24*(10), 816–824. https://doi.org/10.1038/nsmb.3455
789 Jin, W., Wang, J., Liu, C.-P., Wang, H.-W., & Xu, R.-M. (2020). Structural Basis for pri-miRNA
790 Recognition by Drosha. *Molecular Cell*, *78*(3), 423-433.e5.
791 https://doi.org/10.1016/j.molcel.2020.02.024
792 Ketting, R. F., Fischer, S. E., Bernstein, E., Sijen, T., Hannon, G. J., & Plasterk, R. H. (2001). Dicer
793 functions in RNA interference and in synthesis of small RNA involved in developmental
794 timing in C. elegans. *Genes & Development*, *15*(20), 2654–2659.
795 https://doi.org/10.1101/gad.927801
796 Kim, B., Jeong, K., & Kim, V. N. (2017). Genome-wide Mapping of DROSHA Cleavage Sites on
797 Primary MicroRNAs and Noncanonical Substrates. *Molecular Cell*, *66*(2), 258-269.e5.
798 https://doi.org/10.1016/j.molcel.2017.03.013
799 Kim, H., Kim, J., Kim, K., Chang, H., You, K., & Kim, V. N. (2019). Bias-minimized
800 quantification of microRNA reveals widespread alternative processing and 3' end
801 modification. *Nucleic Acids Research*, *47*(5), 2630–2640.
802 https://doi.org/10.1093/nar/gky1293
803 Kim, H., Lee, Y.-Y., & Kim, V. N. (2024). The biogenesis and regulation of animal microRNAs.
804 *Nature Reviews. Molecular Cell Biology*. https://doi.org/10.1038/s41580-024-00805-0
805 Knight, S. W., & Bass, B. L. (2001). A role for the RNase III enzyme DCR-1 in RNA interference
806 and germ line development in Caenorhabditis elegans. *Science (New York, N.Y.)*, *293*(5538),
807 2269–2271. https://doi.org/10.1126/science.1062039
808 Kotagama, K., Grimme, A. L., Braviner, L., Yang, B., Sakhawala, R. M., Yu, G., Benner, L. K.,
809 Joshua-Tor, L., & McJunkin, K. (2024). Catalytic residues of microRNA Argonautes play a
810 modest role in microRNA star strand destabilization in C. elegans. *Nucleic Acids Research*,
811 *52*(9), 4985–5001. https://doi.org/10.1093/nar/gkae170
812 Kruesi, W. S., Core, L. J., Waters, C. T., Lis, J. T., & Meyer, B. J. (2013). Condensin controls
813 recruitment of RNA polymerase II to achieve nematode X-chromosome dosage compensation.
814 *ELife*, *2*, e00808. https://doi.org/10.7554/eLife.00808
815 Kwon, S. C., Baek, S. C., Choi, Y.-G., Yang, J., Lee, Y.-S., Woo, J.-S., & Kim, V. N. (2019a).
816 Molecular Basis for the Single-Nucleotide Precision of Primary microRNA Processing.
817 *Molecular Cell*, *73*(3), 505-518.e5. https://doi.org/10.1016/j.molcel.2018.11.005
818 Kwon, S. C., Baek, S. C., Choi, Y.-G., Yang, J., Lee, Y.-S., Woo, J.-S., & Kim, V. N. (2019b).
819 Molecular Basis for the Single-Nucleotide Precision of Primary microRNA Processing.
820 *Molecular Cell*, *73*(3), 505-518.e5. https://doi.org/10.1016/j.molcel.2018.11.005
821 Kwon, S. C., Nguyen, T. A., Choi, Y.-G., Jo, M. H., Hohng, S., Kim, V. N., & Woo, J.-S. (2016).
822 Structure of Human DROSHA. *Cell*, *164*(1–2), 81–90.
823 https://doi.org/10.1016/j.cell.2015.12.019
824 Landgraf, P., Rusu, M., Sheridan, R., Sewer, A., Iovino, N., Aravin, A., Pfeffer, S., Rice, A.,
825 Kamphorst, A. O., Landthaler, M., Lin, C., Socci, N. D., Hermida, L., Fulci, V., Chiaretti, S.,
826 Foà, R., Schliwka, J., Fuchs, U., Novosel, A., … Tuschl, T. (2007). A mammalian microRNA
827 expression atlas based on small RNA library sequencing. *Cell*, *129*(7), 1401–1414.
828 https://doi.org/10.1016/j.cell.2007.04.040
829 Landthaler, M., Yalcin, A., & Tuschl, T. (2004). The human DiGeorge syndrome critical region
830 gene 8 and Its D. melanogaster homolog are required for miRNA biogenesis. *Current Biology :*
831 *CB*, *14*(23), 2162–2167. https://doi.org/10.1016/j.cub.2004.11.001

Langmead, B., & Salzberg, S. L. (2012). Fast gapped-read alignment with Bowtie 2. *Nature Methods*, *9*(4), 357–359. https://doi.org/10.1038/nmeth.1923

Lataniotis, L., Albrecht, A., Kok, F. O., Monfries, C. A. L., Benedetti, L., Lawson, N. D., Hughes, S. M., Steinhofel, K., Mayr, M., & Zampetaki, A. (2017). CRISPR/Cas9 editing reveals novel mechanisms of clustered microRNA regulation and function. *Scientific Reports*, *7*(1), 8585. https://doi.org/10.1038/s41598-017-09268-0

Lee, Y., Ahn, C., Han, J., Choi, H., Kim, J., Yim, J., Lee, J., Provost, P., Rådmark, O., Kim, S., & Kim, V. N. (2003). The nuclear RNase III Drosha initiates microRNA processing. *Nature*, *425*(6956), 415–419. https://doi.org/10.1038/nature01957

Lee, Y., Kim, M., Han, J., Yeom, K.-H., Lee, S., Baek, S. H., & Kim, V. N. (2004). MicroRNA genes are transcribed by RNA polymerase II. *The EMBO Journal*, *23*(20), 4051–4060. https://doi.org/10.1038/sj.emboj.7600385

Li, S., Nguyen, T. D., Nguyen, T. L., & Nguyen, T. A. (2020). Mismatched and wobble base pairs govern primary microRNA processing by human Microprocessor. *Nature Communications*, *11*(1), 1926. https://doi.org/10.1038/s41467-020-15674-2

Li, S., Nguyen, T. D., Nguyen, T. L., & Nguyen, T. A. (2021). Author Correction: Mismatched and wobble base pairs govern primary microRNA processing by human Microprocessor. *Nature Communications*, *12*(1), 6255. https://doi.org/10.1038/s41467-021-26533-z

Love, M. I., Huber, W., & Anders, S. (2014). Moderated estimation of fold change and dispersion for RNA-seq data with DESeq2. *Genome Biology*, *15*(12), 550. https://doi.org/10.1186/s13059-014-0550-8

Lund, E., Güttinger, S., Calado, A., Dahlberg, J. E., & Kutay, U. (2004). Nuclear export of microRNA precursors. *Science (New York, N.Y.)*, *303*(5654), 95–98. https://doi.org/10.1126/science.1090599

Mandlbauer, A., Sun, Q., Popitsch, N., Schwickert, T., Spanova, M., Wang, J., Ameres, S. L., Busslinger, M., & Cochella, L. (2024). Mime-seq 2.0: a method to sequence microRNAs from specific mouse cell types. *The EMBO Journal*, *43*(12), 2506–2525. https://doi.org/10.1038/s44318-024-00102-8

Martinez, N. J., Ow, M. C., Reece-Hoyes, J. S., Barrasa, M. I., Ambros, V. R., & Walhout, A. J. M. (2008). Genome-scale spatiotemporal analysis of Caenorhabditis elegans microRNA promoter activity. *Genome Research*, *18*(12), 2005–2015. https://doi.org/10.1101/gr.083055.108

Merritt, C., Rasoloson, D., Ko, D., & Seydoux, G. (2008). 3' UTRs are the primary regulators of gene expression in the C. elegans germline. *Current Biology : CB*, *18*(19), 1476–1482. https://doi.org/10.1016/j.cub.2008.08.013

Mészáros, B., Erdos, G., & Dosztányi, Z. (2018). IUPred2A: context-dependent prediction of protein disorder as a function of redox state and protein binding. *Nucleic Acids Research*, *46*(W1), W329–W337. https://doi.org/10.1093/nar/gky384

Mitrea, D. M., & Kriwacki, R. W. (2016). Phase separation in biology; functional organization of a higher order. *Cell Communication and Signaling : CCS*, *14*, 1. https://doi.org/10.1186/s12964-015-0125-7

Mourelatos, Z., Dostie, J., Paushkin, S., Sharma, A., Charroux, B., Abel, L., Rappsilber, J., Mann, M., & Dreyfuss, G. (2002). miRNPs: a novel class of ribonucleoproteins containing numerous microRNAs. *Genes & Development*, *16*(6), 720–728. https://doi.org/10.1101/gad.974702

Nguyen, T. A., Jo, M. H., Choi, Y.-G., Park, J., Kwon, S. C., Hohng, S., Kim, V. N., & Woo, J.-S. (2015). Functional Anatomy of the Human Microprocessor. *Cell*, *161*(6), 1374–1387. https://doi.org/10.1016/j.cell.2015.05.010

Nguyen, T. L., Nguyen, T. D., Ngo, M. K., Le, T. N.-Y., & Nguyen, T. A. (2023). Noncanonical processing by animal Microprocessor. *Molecular Cell*, *83*(11), 1810-1826.e8. https://doi.org/10.1016/j.molcel.2023.05.004

Nguyen, T. L., Nguyen, T. D., Ngo, M. K., & Nguyen, T. A. (2023). Dissection of the Caenorhabditis elegans Microprocessor. *Nucleic Acids Research*, *51*(4), 1512–1527. https://doi.org/10.1093/nar/gkac1170

Paix, A., Wang, Y., Smith, H. E., Lee, C. Y. S., Calidas, D., Lu, T., Smith, J., Schmidt, H., Krause, M. W., & Seydoux, G. (2014). Scalable and versatile genome editing using linear DNAs with microhomology to Cas9 sites in Caenorhabditis elegans. *Genetics*, *198*(4), 1347–1356. https://doi.org/10.1534/genetics.114.170423

Pantano, L., Estivill, X., & Martí, E. (2010). SeqBuster, a bioinformatic tool for the processing and analysis of small RNAs datasets, reveals ubiquitous miRNA modifications in human embryonic cells. *Nucleic Acids Research*, *38*(5), e34. https://doi.org/10.1093/nar/gkp1127

Partin, A. C., Ngo, T. D., Herrell, E., Jeong, B.-C., Hon, G., & Nam, Y. (2017). Heme enables proper positioning of Drosha and DGCR8 on primary microRNAs. *Nature Communications*, *8*(1), 1737. https://doi.org/10.1038/s41467-017-01713-y

Partin, A. C., Zhang, K., Jeong, B.-C., Herrell, E., Li, S., Chiu, W., & Nam, Y. (2020). Cryo-EM Structures of Human Drosha and DGCR8 in Complex with Primary MicroRNA. *Molecular Cell*, *78*(3), 411-422.e4. https://doi.org/10.1016/j.molcel.2020.02.016

Pawlicki, J. M., & Steitz, J. A. (2008). Primary microRNA transcript retention at sites of transcription leads to enhanced microRNA production. *The Journal of Cell Biology*, *182*(1), 61–76. https://doi.org/10.1083/jcb.200803111

Pham, K., Masoudi, N., Leyva-Díaz, E., & Hobert, O. (2021). A nervous system-specific subnuclear organelle in Caenorhabditis elegans. *Genetics*, *217*(1), 1–17. https://doi.org/10.1093/genetics/iyaa016

Piuco, R., & Galante, P. A. F. (2021). *piRNAdb: A piwi-interacting RNA database*. https://doi.org/10.1101/2021.09.21.461238

Prabhakar, A., Hu, S., Tang, J., Ghatpande, P., Lagna, G., Jiang, X., & Hata, A. (2023). Essential role of the amino-terminal region of Drosha for the Microprocessor function. *IScience*, *26*(10), 107971. https://doi.org/10.1016/j.isci.2023.107971

Putnam, A., Thomas, L., & Seydoux, G. (2023). RNA granules: functional compartments or incidental condensates? *Genes & Development*, *37*(9–10), 354–376. https://doi.org/10.1101/gad.350518.123

Putri, G. H., Anders, S., Pyl, P. T., Pimanda, J. E., & Zanini, F. (2022). Analysing high-throughput sequencing data in Python with HTSeq 2.0. *Bioinformatics (Oxford, England)*, *38*(10), 2943–2945. https://doi.org/10.1093/bioinformatics/btac166

Reinhart, B. J., Slack, F. J., Basson, M., Pasquinelli, A. E., Bettinger, J. C., Rougvie, A. E., Horvitz, H. R., & Ruvkun, G. (2000). The 21-nucleotide let-7 RNA regulates developmental timing in Caenorhabditis elegans. *Nature*, *403*(6772), 901–906. https://doi.org/10.1038/35002607

Saito, T. L., Hashimoto, S., Gu, S. G., Morton, J. J., Stadler, M., Blumenthal, T., Fire, A., & Morishita, S. (2013). The transcription start site landscape of C. elegans. *Genome Research*, *23*(8), 1348–1361. https://doi.org/10.1101/gr.151571.112

Sakhawala, R. M., Tirgar, R., Vieux, K.-F., Haskell, D., Yu, G., Zinovyeva, A., & McJunkin, K. (2025). A noncanonical Pol III-dependent, Microprocessor-independent biogenesis pathway generates a germline-enriched miRNA family. *Genes & Development*. https://doi.org/10.1101/gad.352481.124

Shang, R., Baek, S. C., Kim, K., Kim, B., Kim, V. N., & Lai, E. C. (2020). Genomic Clustering Facilitates Nuclear Processing of Suboptimal Pri-miRNA Loci. *Molecular Cell*, *78*(2), 303-316.e4. https://doi.org/10.1016/j.molcel.2020.02.009

Slezak-Prochazka, I., Kluiver, J., de Jong, D., Kortman, G., Halsema, N., Poppema, S., Kroesen, B.-J., & van den Berg, A. (2013). Cellular localization and processing of primary transcripts of exonic microRNAs. *PloS One*, *8*(9), e76647. https://doi.org/10.1371/journal.pone.0076647

Smith, T., Heger, A., & Sudbery, I. (2017). UMI-tools: modeling sequencing errors in Unique Molecular Identifiers to improve quantification accuracy. *Genome Research*, *27*(3), 491–499. https://doi.org/10.1101/gr.209601.116

Son, S., Kim, B., Yang, J., & Kim, V. N. (2023). Role of the proline-rich disordered domain of DROSHA in intronic microRNA processing. *Genes & Development*, *37*(9–10), 383–397. https://doi.org/10.1101/gad.350275.122

Sternberg, P. W., Van Auken, K., Wang, Q., Wright, A., Yook, K., Zarowiecki, M., Arnaboldi, V., Becerra, A., Brown, S., Cain, S., Chan, J., Chen, W. J., Cho, J., Davis, P., Diamantakis, S., Dyer, S., Grigoriadis, D., Grove, C. A., Harris, T., … Stein, L. (2024). WormBase 2024: status and transitioning to Alliance infrastructure. *Genetics*, *227*(1). https://doi.org/10.1093/genetics/iyae050

Stiernagle, T. (2006). Maintenance of C. elegans. *WormBook : The Online Review of C. Elegans Biology*, 1–11. https://doi.org/10.1895/wormbook.1.101.1

Tabara, H., Sarkissian, M., Kelly, W. G., Fleenor, J., Grishok, A., Timmons, L., Fire, A., & Mello, C. C. (1999). The rde-1 gene, RNA interference, and transposon silencing in C. elegans. *Cell*, *99*(2), 123–132. https://doi.org/10.1016/s0092-8674(00)81644-x

Thivierge, C., Bellefeuille, M., Diwan, S.-S., Dyakov, B. J. A., Leventis, R., Perron, G., Najafabadi, H. S., Gravel, S.-P., Gingras, A.-C., & Duchaine, T. F. (2024). Paraspeckle-independent co-transcriptional regulation of nuclear microRNA biogenesis by SFPQ. *Cell Reports*, *43*(9), 114695. https://doi.org/10.1016/j.celrep.2024.114695

Truscott, M., Islam, A. B. M. M. K., & Frolov, M. V. (2016). Novel regulation and functional interaction of polycistronic miRNAs. *RNA (New York, N.Y.)*, *22*(1), 129–138. https://doi.org/10.1261/rna.053264.115

Vieux, K.-F., Prothro, K. P., Kelley, L. H., Palmer, C., Maine, E. M., Veksler-Lublinsky, I., & McJunkin, K. (2021). Screening by deep sequencing reveals mediators of microRNA tailing in C. elegans. *Nucleic Acids Research*, *49*(19), 11167–11180. https://doi.org/10.1093/nar/gkab840

Wang, X., Jiang, Q., Zhang, H., He, Z., Song, Y., Chen, Y., Tang, N., Zhou, Y., Li, Y., Antebi, A., Wu, L., Han, J.-D. J., & Shen, Y. (2024). Tissue-specific profiling of age-dependent miRNAomic changes in Caenorhabditis elegans. *Nature Communications*, *15*(1), 955. https://doi.org/10.1038/s41467-024-45249-4

Witten, G., DeMott, E., Huang, G., Zelasko, F., de Jesus, B., Mulchand, C., Schuck, L., Pullman, S., Perez, A., Mahableshwarkar, P., Wu, Z., Cardona, E. A., Pierce, J. T., Dickinson, D. J., & Doonan, R. (2023). mScarlet and split fluorophore mScarlet resources for plasmid-based

CRISPR/Cas9 knock-in in C. elegans. *MicroPublication Biology*, *2023*. https://doi.org/10.17912/micropub.biology.000871

Yang, B., Schwartz, M., & McJunkin, K. (2020). In vivo CRISPR screening for phenotypic targets of the mir-35-42 family in C. elegans. *Genes & Development* , *34*(17–18), 1227–1238. https://doi.org/10.1101/gad.339333.120

Yi, R., Qin, Y., Macara, I. G., & Cullen, B. R. (2003). Exportin-5 mediates the nuclear export of pre-microRNAs and short hairpin RNAs. *Genes & Development*, *17*(24), 3011–3016. https://doi.org/10.1101/gad.1158803

Zeng, Y., & Cullen, B. R. (2004). Structural requirements for pre-microRNA binding and nuclear export by Exportin 5. *Nucleic Acids Research*, *32*(16), 4776–4785. https://doi.org/10.1093/nar/gkh824

Zeng, Y., Yi, R., & Cullen, B. R. (2005). Recognition and cleavage of primary microRNA precursors by the nuclear processing enzyme Drosha. *The EMBO Journal*, *24*(1), 138–148. https://doi.org/10.1038/sj.emboj.7600491

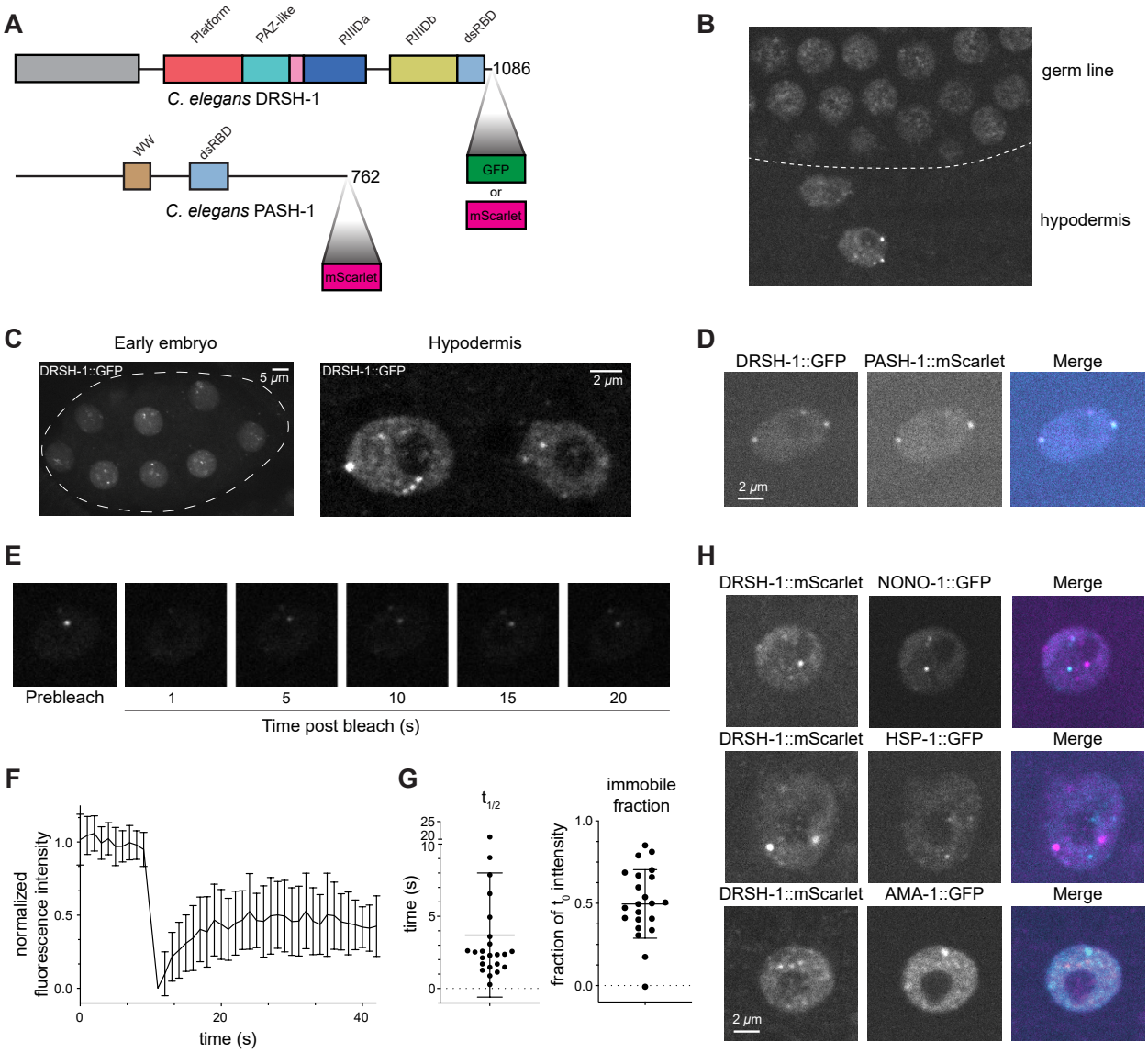

Figure 1. Microprocessor forms distinct nuclear granules in select tissues. (A) Domain architecture of *C. elegans* DRSH-1 and PASH-1. GFP and mScarlet were fused to DRSH-1 and PASH-1 at the C-terminus endogenously via CRISPR/Cas9. RIIID = RNase III domain, dsRBD = dsRNA binding domain. (B) Micrograph showing DRSH-1::GFP in germline nuclei lacking foci (top) and hypodermis nuclei containing foci (bottom). (C) Representative micrographs of DRSH-1::GFP in early embryos (left) and two hypodermal nuclei (right). Left: Dotted line outlines the embryo structure. Right: The large nucleoli characteristic of hypodermal nuclei exclude DRSH-1::GFP. Maximum intensity projection. (D) Representative images of co-localization of DRSH-1::GFP and PASH-1::mScarlet in a hypodermal cell. Single z plane shown. (E) Time-lapse images show fluorescence recovery of DRSH-1::GFP after a single focus is photobleached at 1.0 sec. Single z plane shown (F) FRAP recovery curves for DRSH-1::GFP. Data is reported as a mean +/- SD (n = 23 granules). (G) Half recovery time and immobile fraction were calculated based on fitted FRAP recovery curves for individual foci as shown in figure E. Bars are mean +/- SD. (H)

Representative images show co-labeling of DRSH-1::GFP and known nuclear granule markers. Maximum intensity projections.

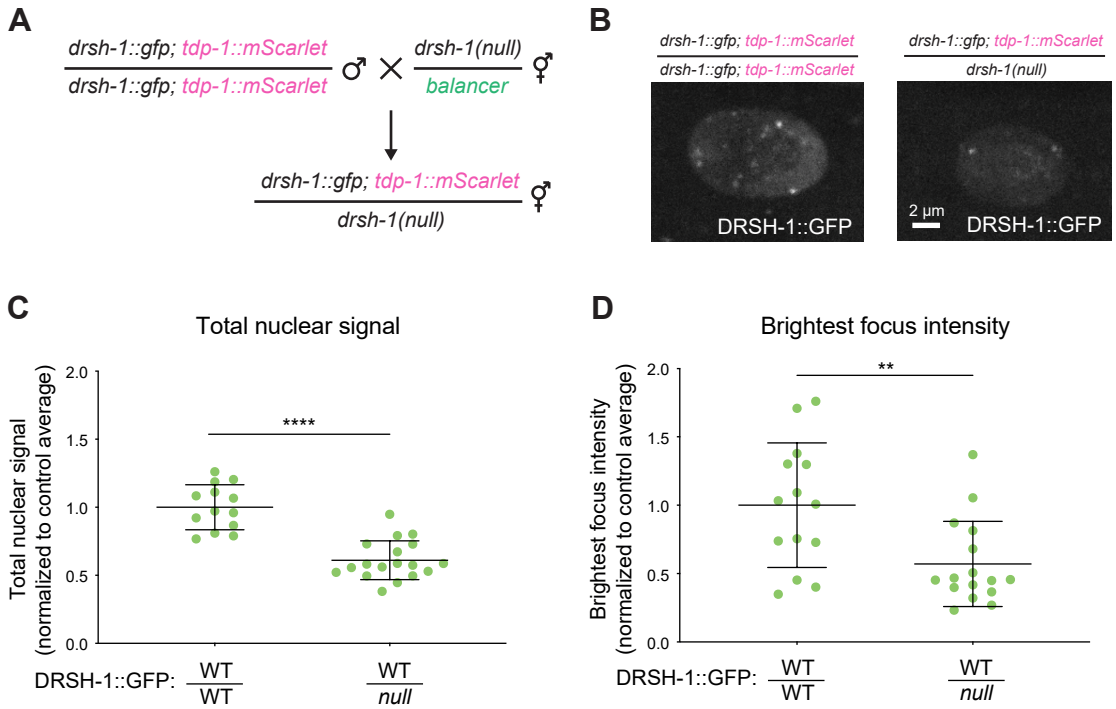

Figure 2. DRSH-1 granules are not strictly dependent on saturation concentration of DRSH-1. (A) Schematic of the genetic cross to generate *drsh-1::gfp/drsh-1(null)* heterozygous. *tdp-1::mScarlet* is a visual marker to differentiate cross progeny from self-progeny. Heterozygous worms were selected based on the visual marker. *drsh-1::gfp;tdp-1::mScarlet* homozygous worms were collected and used as control. (B) Representative images of DRSH-1::GFP in hypodermal cells in genetic background containing two (left) or one (right) allele of DRSH-1::GFP. Maximum intensity projection. (C) Quantification of the total nuclear signal of DRSH-1::GFP. (D) Quantification of the signal intensity of the brightest focus per nucleus across indicated genotypes in hypodermal cells. (C-D) N ≥ 6 animals per genotype. Signal is normalized to the average signal in the control genotype (homozygous DRSH-1::GFP).

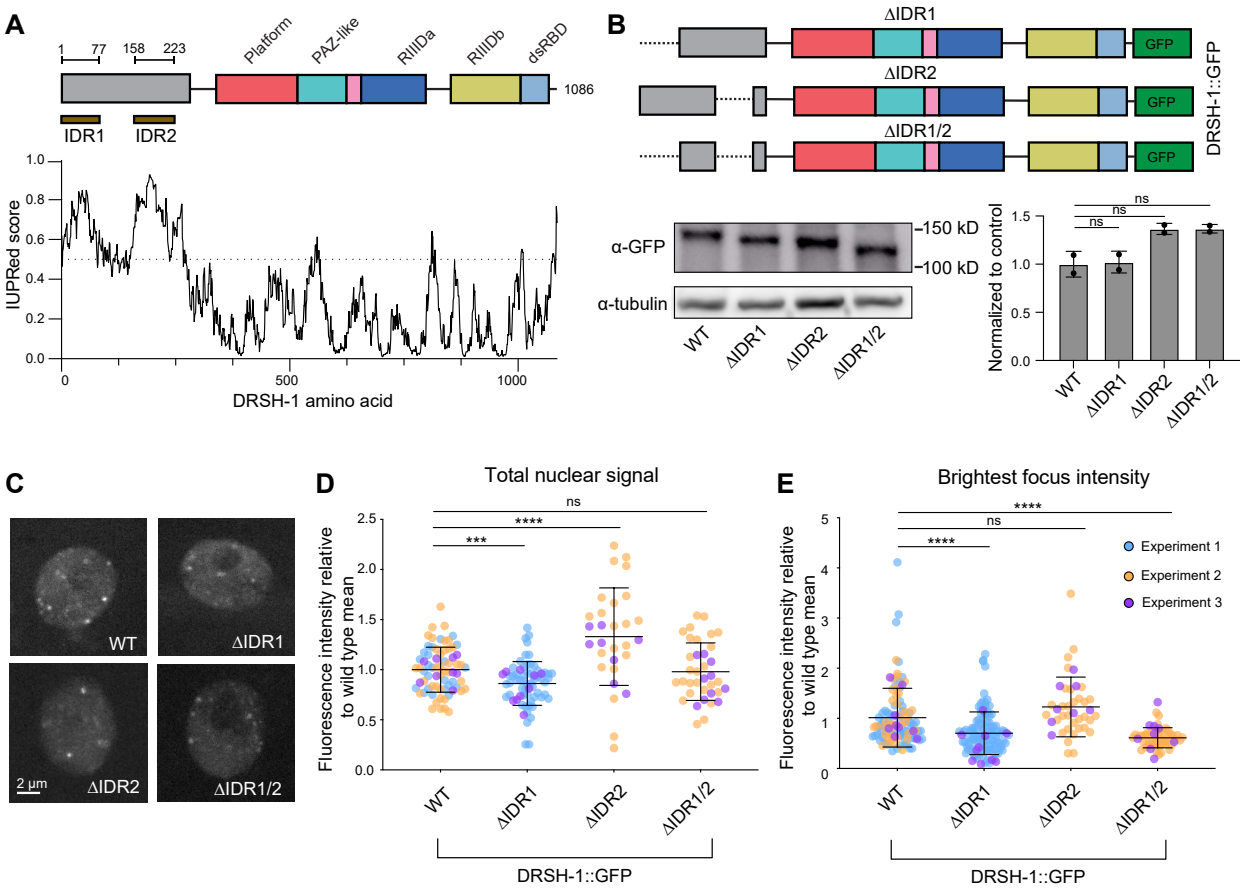

Figure 3. Deletion of N-terminal IDRs reduces but does not abolish DRSH-1 granule recruitment. (A) IUPRed was used to predict two intrinsically disordered domains: IDR1 (A.A. 1-77) and IDR2 (A.A. 158-233). (B) Schematics of IDR deletions generated in the *drsh-1::gfp* background using CRISPR/Cas9 and representative western blot images to show truncations of the DRSH-1::GFP fusion proteins in whole animal samples. Western quantification was normalized first to tubulin and then compared to wild type. Two tailed unpaired Student's test: ns, not significant. (C) Representative images of DRSH-1::GFP signal in hypodermal nuclei across different genotypes. Maximum intensity projections. (D) Super plot showing the quantification of total nuclear signal of DRSH-1::GFP. (E) Super plot showing the quantification of the intensity of the brightest focus in each nucleus. (D-E) N ≥ 15 animals per genotype combining three experiments. Signal is normalized to the average signal in the control genotype (wild type DRSH-1::GFP) from the same imaging session. Data are color-coded by imaging session.

A

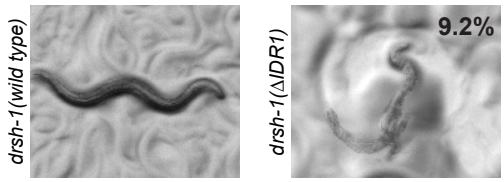

B

	number burst animals	n	percent bursting
drsh-1(wild type)	0	100	0.0%
drsh-1(ΔIDR1)	55	599	9.2%
drsh-1(ΔIDR2)	0	289	0.0%
drsh-1::gfp(wild type)	0	234	0.0%
drsh-1::gfp(ΔIDR1)	24	228	10.5%
drsh-1::gfp(ΔIDR2)	0	331	0.0%
drsh-1::gfp(ΔIDR1/2)	18	184	9.8%

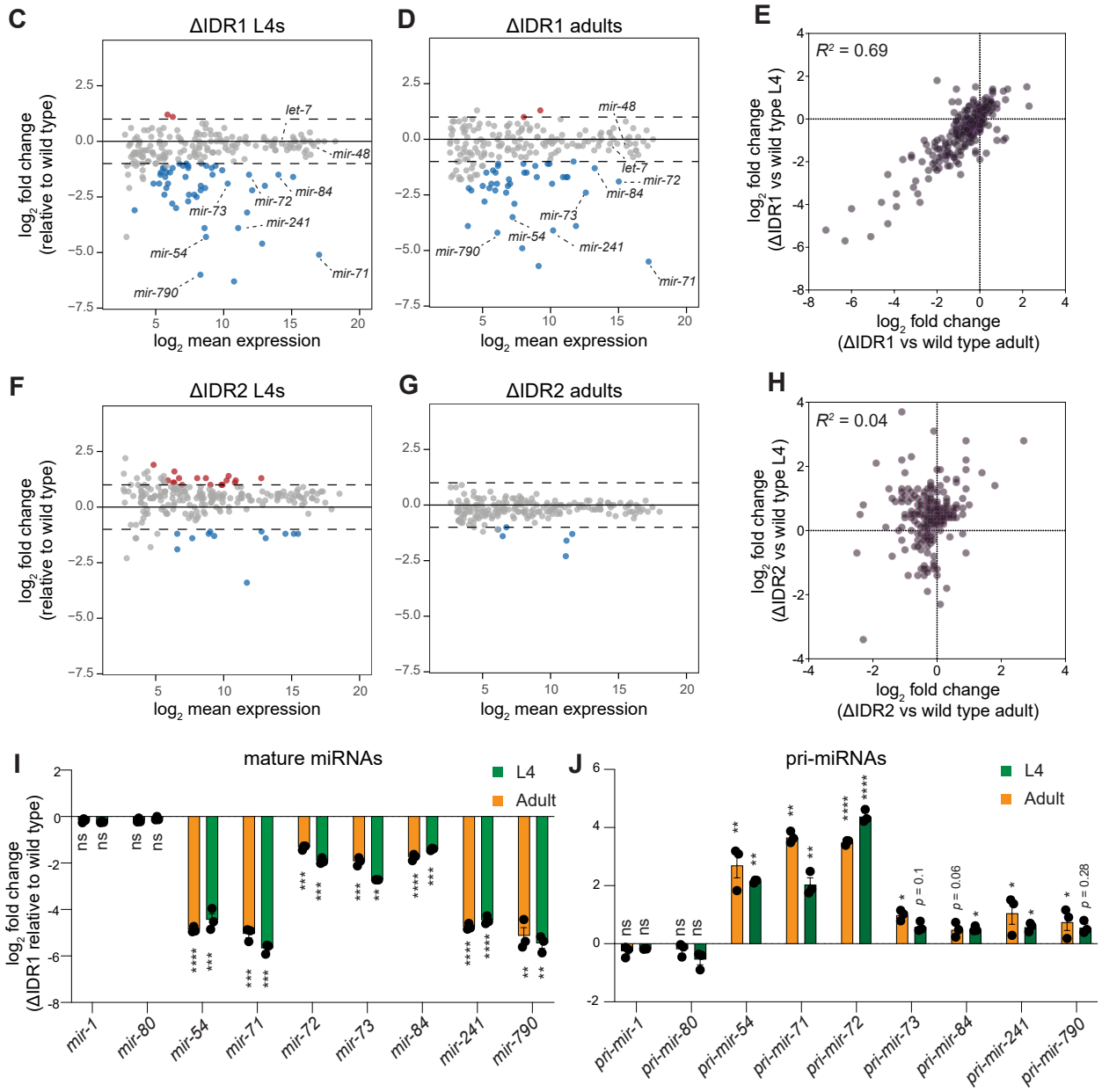

Figure 4. DRSH-1 IDR1 is important for the biogenesis of a subset of miRNAs. (A) Representative images showing the bursting phenotypes observed in 9.2% of ΔIDR1 young adult animals. (B) Table listing the penetrance of the bursting phenotype in different genotypes. IDR deletions were generated in both wild type and *drsh-1::gfp* backgrounds. (C-D, F-G) MA plots

showing average abundance on the X-axis and the log_2fold change on the Y-axis. Sequencing analysis results were obtained from DESeq2 using total piRNA reads for normalization. miRNAs showing significant changes compared to wild type of the same stage are shown in blue (downregulated, log_2fold change < -1 and $p_{adj} < 0.05$) and red (upregulated, log_2fold change > 1 and $p_{adj} < 0.05$. (C and D) MA plots showing miRNA abundance changes in ΔIDR1 versus wild type for L4 and adult, respectively (E) X-Y plot showing the correlation of log_2fold change for ΔIDR1/wild type between L4 (Y-axis) and adult (X-axis). (F and G) MA plots showing miRNA abundance changes in ΔIDR2 versus wild type for L4 and adult, respectively. (H) X-Y plot showing the correlation of log_2fold change for ΔIDR2/wild type between L4 and adult samples. (I) Relative levels of mature miRNAs as measured by Taqman qPCR in ΔIDR1 L4 and adults, normalized to wild type of the same stage. (J) Relative levels of primary miRNA transcripts as measured by qRT-PCR in ΔIDR1 L4 and adults, normalized to wild type of the same stage. (I-J) *Sn2429* and *gpd-1* were used as internal controls for mature miRNAs and pri-miRNAs, respectively. Two tailed unpaired Student's test: (*) P < 0.05, (**) P < 0.01, (***) P < 0.001, (****) P < 0.0001.

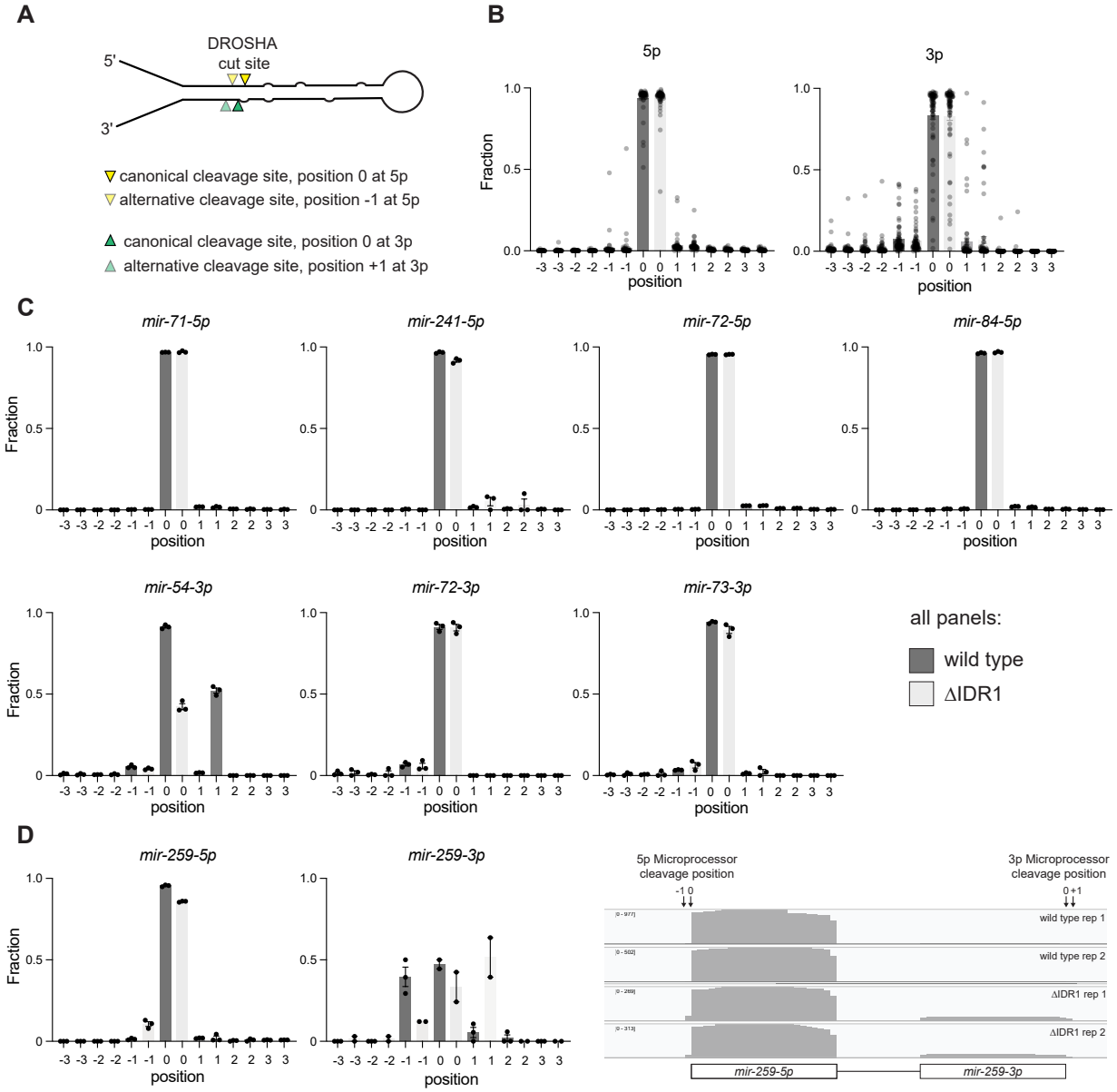

Figure 5. DRSH-1 IDR1 has almost no effect on Microprocessor precision. (A) Illustration of pri-miRNA showing an example of relative positions of canonical and alternative Microprocessor cleavage sites. (B) Distribution of terminal miRNA positions for 5′ ends of 5p miRNA strands and 3′ ends of 3p strands in wild type and *drsh-1(ΔIDR1)* animals at adult stage. (C) Examples of 5p and 3p strand isomiR distribution of individual miRNAs. These miRNAs are downregulated significantly in abundance in the *drsh-1(ΔIDR1)* animals. (D) isomiR distribution of both strands of *mir-259* showing decreased precision in the Δ*IDR1* background.

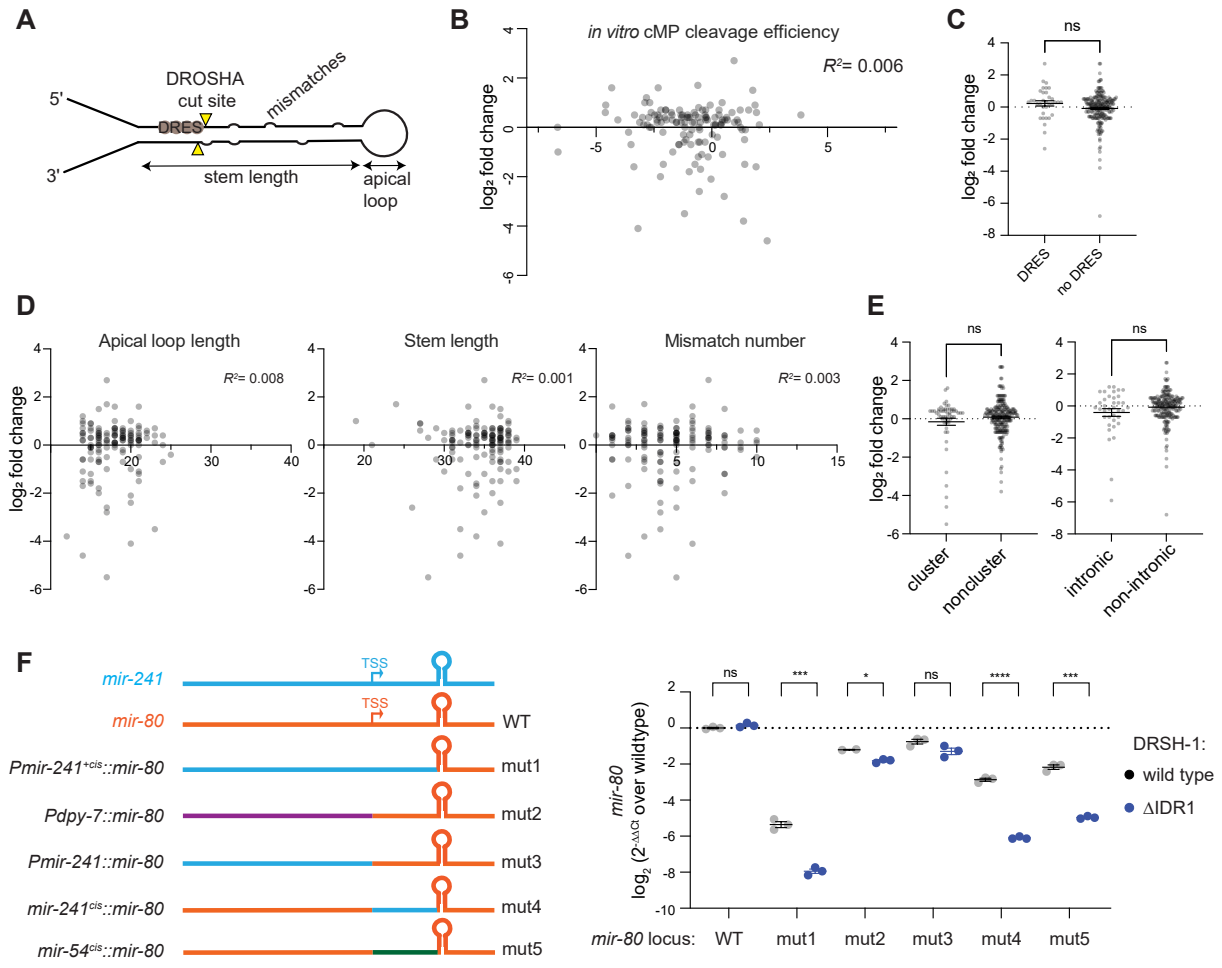

Figure 6. 5′ flanking sequence of miRNA confers IDR1-sensitivity. (A) Schematic diagram of local features of a pri-miRNA hairpin. (B) X-Y plot showing correlation between IDR1 sensitivity measured by miRNA $\log_2$ fold change (ΔIDR1/wild type L4) on the Y-axis and *in vitro C. elegans* Microprocessor cleavage efficiency from Nguyen, et al. 2023 on the X-axis. (C, E) IDR1 sensitivity between miRNA groups based on classifications: containing DROSHA dsRNA recognition sites (DRES) site or not in (C), clustering or standalone and intronic or exonic in (E). Two tailed unpaired Student's t-test, ns, not significant. (D) X-Y plots showing correlation between IDR1 sensitivity, and different predicted pri-miRNA secondary features, including apical loop length, stem length and mismatch number. (F) Left: Schematics showing genome edits made at the *mir-80* locus. Genomic structure of *pri-mir-241* is shown in blue, and orange shows the genomic structure of *pri-mir-80*. Hairpin structure depicts the pri-miRNA hairpin defined by the basal junctions. TSS denotes transcription start site. Right: *mir-80* Taqman qPCR comparing different mutants in DRSH-1 wild type or ΔIDR1 background at adult stage. Two-tailed unpaired Student's t-test: (ns) not significant, (*) $P < 0.05$, (**) $P < 0.01$, (***) $P < 0.001$, (****) $P < 0.0001$.

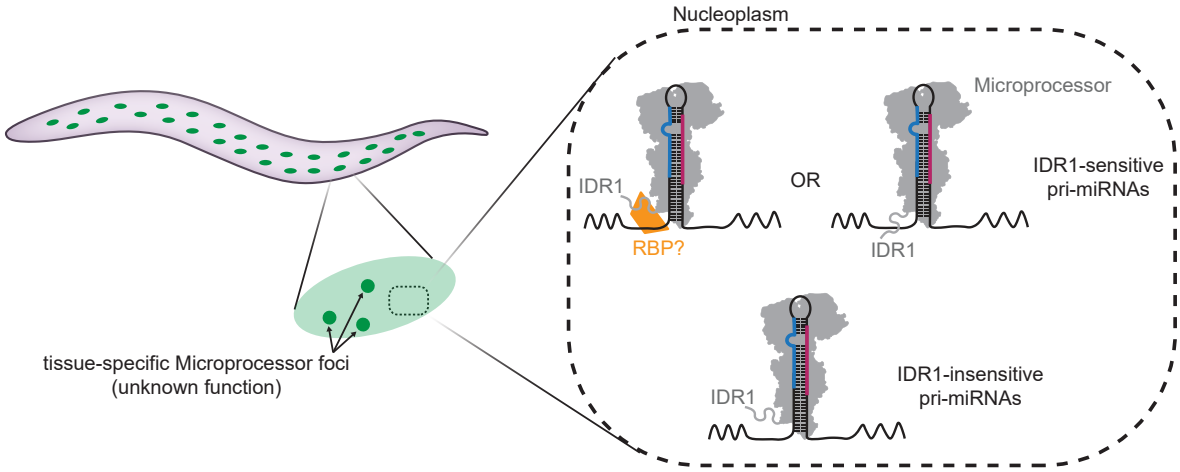

Figure 7. Model of DRSH-1 IDR1 function. Left: Microprocessor forms distinct foci in select tissues, such as hypodermis. Right: DRSH-1 IDR1 functions in miRNA maturation independent of Microprocessor focus formation. Sequences flanking the pri-miRNA hairpin confer sensitivity to the presence of IDR1. IDR1 may interact directly or indirectly with sequences flanking the pri-miRNA hairpin to promote Microprocessing.